Supplementary Information (SI) for Journal of Materials Chemistry A.

Supplementary Information for:

Elucidating conductivity and nitriding resiliency in (Al/H)-ZnO coatings for NH_3-fueled SOFC separators *via* SEM-EDX and MLP-DFT protocols

Matthew T. Curnan[1,*], Kyung Chan Min[2,*], Joon Hyung Shim[2,†], Geun Ho Gu[1,†]

Affiliations:

[1] Department of Energy Engineering, Korea Institute of Energy Technology (KENTECH), 21 Kentech-gil, Naju 58330, Republic of Korea

[2] Department of Mechanical Engineering, Korea University, 145 Anam-ro, Seongbuk-gu, Seoul 02841, Republic of Korea

[†] Corresponding author(s) e-mail: ggu@kentech.ac.kr (G.H.G.), shimm@korea.ac.kr (J. H. S.)

[*] These authors contributed equally to this work

Expanded computational methodology

General simulation

All Density Functional Theory (DFT) simulations in this paper were completed via the Vienna *Ab Initio* Simulation Package (VASP; version 6.4.3),[1] while all simulations performed via a universal machine learning potential (MLP) were performed with the Crystal Hamiltonian Graph neural NETwork (CHGNET).[2] Unless otherwise stated, DFT calculations employed the Perdew-Burke-Ernzerhof (PBE) parameterization of the Generalized Gradient Approximation (GGA) functional,[3,4] as well as standard PAW pseudopotentials (labelled 'Al', 'Zn', 'O', and 'N' in VASP).[5] By default, DFT calculations applied an energy cutoff (ENCUT) of 550 eV and spin polarization (ISPIN = 2), as well as respective energy (EDIFF) and force (EDIFFG) relaxation tolerances of $5x10^{-5}$ eV and 0.02 eV/Å.[6–8] Bulk and surface structures were respectively relaxed without (ISIF = 3) and with (ISIF = 2) volumetric and cell dimension constraints.[6,9,10] For DFT energetics associated with bulk cell dimensions in CHGNET-DFT validation, phase diagram, and H insertion simulations, Gamma-centered *k*-point grids were applied according to a unitary reference, or 8x8x8 for a bulk cell with dimensions of 3 Å in all directions.[10] Within computational limits, this was multiplicatively scaled down with expanding bulk cell dimensions in larger materials systems. Dimensions of molecular and surface simulation cells featuring vacuum all assigned corresponding *k*-point grid dimensions of 1.[10] With respect to electronic structure calculations completed on bulk hexagonal ZnO ($\boldsymbol{P}6_3mc$) and associated Al-doped ZnO (AZO) configurations, *k*-points were applied similarly with a 12x12x12 reference *k*-point grid.[11–13]

For surface and interfacial DFT calculations completed on Zn(0001) (generated from bulk Zn, $P6_3/mmc$) and ZnO(0001) systems, slabs were respectively built using four and six layers.[14–17] Half of these were fixed for both Zn(0001) (2 layers) and ZnO(0001) (3 layers) surfaces, while each slab imposed a vacuum (along *z*-axis) of at least 20 Å.[18–20] For simulations involving N surface and subsurface adsorption on Zn(0001) slabs, energetic convergence was reached within 0.01 eV between interfacial (*x* and *y* axes) supercell dimensions of 3x3 and 4x4. Thus, for all NH_x (x=0-3) adsorption slab results excluding convergence testing, as well as electronic structure and conductivity evaluations of ZnO slabs, 4x4 supercell dimensions were implemented.[21] For each AZO simulation, a single Al substitutes Zn on a Zn site, while different Al concentrations are tested by expanding supercell size relative to the ZnO unit cell.[11] With respect to Al-impurity concentration (Al at. %) across all cationic sites, the following AZO systems were simulated in this paper, with cell dimensions defined according to supercells of the pristine ZnO unit cell (4 atoms):[12,13]

Dimensions	Stoichiometry	Al at. %	Dimensions	Stoichiometry	Al at. %
2x2x1	$Al_1Zn_7O_8$	12.5%	6x2x2	$Al_1Zn_{47}O_{48}$	2.08%
3x2x1	$Al_1Zn_{11}O_{12}$	8.33%	3x3x3	$Al_1Zn_{53}O_{54}$	1.85%
2x2x2	$Al_1Zn_{15}O_{16}$	6.25%	4x4x2	$Al_1Zn_{63}O_{64}$	1.56%
3x2x2	$Al_1Zn_{23}O_{24}$	4.16%	4x3x3	$Al_1Zn_{71}O_{72}$	1.39%
4x2x2	$Al_1Zn_{31}O_{32}$	3.13%	5x4x2	$Al_1Zn_{79}O_{80}$	1.25%
5x2x2	$Al_1Zn_{39}O_{40}$	2.50%	4x4x3	$Al_1Zn_{95}O_{96}$	1.04%

Simulations involving H insertion or incorporation were done on 3x3x2 bulk ZnO supercells.[22,23] All DFT molecular energies – encompassing those of NH_x (x=0-3), N_2, H_2, and O_2 – employed as chemical potentials or otherwise were resolved via single *k*-point calculations, namely within simulation boxes featuring edge lengths of 15 Å.[6] Corresponding CHGNET energies – which effectively serve as molecular chemical potentials in analogous calculations – were calculated by adapting structures from the Materials Project (MP) database with corresponding stoichiometries, including NH_3 (mp-29145), N_2 (mp-154), H_2 (mp-730101), and O_2 (mp-723285).[8,24]

General formation energies (E_f) resolved for CHGNET-DFT cross-validation, related phase diagrams, and other connected calculations (unless otherwise noted) were resolved via the formalism:[25]

$$E_f = \frac{1}{N}\left(E_{total} - \sum_{j}^{J} m_j E_j\right) \quad [1]$$

For both CHGNET and DFT, E_f are achieved from the total relaxed energies (E_{total}) of materials systems within the Al-Zn-N-O phase space, differenced relative to corresponding elemental or atomic energies (E_j) weighted by their stoichiometric proportions within such systems (m_j). For each materials system, each present element (j) is considered over the total set of all elements (J = {Al, Zn, N, O}). Each E_f is normalized with respect to the total number of atoms comprising its matching materials system (N). Formation energies for inserting 1-4 (n=1-4) interstitial H ($E_{f,int}$) are resolved for $1H_i$ (Figure S21), $2H_i$ (Figure S22), V_{Zn}-nH (Figure S23), and V_O-nH (Figure S24) systems using the following equation:[23,26,27]

$$E_{f,int} = \frac{1}{N}\left(E_{H-ZnO} - E_{ZnO,ref} - \frac{n}{2}\left[E_{H_2} + E_{corr,H_2}\right]\right) \quad [2]$$

Here, $E_{f,int}$ is calculated from the relaxed DFT energies of a ZnO-based reference structure ($E_{ZnO,ref}$), that reference structure containing a particular H interstitial configuration ($E_{H\text{-}ZnO}$), isolated molecular H_2 (E_{H2}), a corrective term for E_{H2} described in the following subsection *Nitride Screening and Phase Diagrams* ($E_{corr,H2}$), and the total number of atoms comprising a given simulation (N). For systems without vacancies, $E_{ZnO,ref}$ represents a pristine bulk ZnO crystallographic structure (E_{ZnO}), while it represents bulk ZnO with one Zn or O vacancy (E_{vac}) for materials containing such defects. Corresponding O or Zn vacancy formation energies (ΔE_{vac}) are yielded using the following expression:[6]

$$\Delta E_{vac} = E_{vac} - E_{ZnO} + E_{mol,ref} \quad [3]$$

Here, ΔE_{vac} is produced from E_{ZnO}, E_{vac}, and the relaxed DFT energy of a molecular reference matching the type of defect induced. For Zn and O vacancy defects, this is either bulk Zn (E_{Zn}) or molecular O_2 (E_{O2}) normalized per-atom, respectively. Combining the two equations above – while using E_{vac} for $E_{ZnO,ref}$ – develops the total formation energy comprising both interstitial H and Zn/O vacancy defect formation ($\Delta E_{vac,int}$), as described through the following equation:

$$\Delta E_{vac,int} = NE_{f,int} + \Delta E_{vac} = E_{H-ZnO} - \frac{n}{2}\left[E_{H_2} + E_{corr,H_2}\right] + E_{vac} - E_{ZnO} \quad [4]$$

Adsorption energies for NH_x (x=0-3) surface configurations (E_{ads}) were calculated as follows:[21]

$$E_{ads} = E_{surf-NH_x} - E_{NH_x} - E_{surf} \quad [5]$$

Here, E_{ads} were yielded through the relaxed DFT energies of Zn(0001) or ZnO(0001) surfaces (E_{surf}), isolated NH_x molecules or N atoms (E_{NHx}), and corresponding NH_x adsorbates on such surfaces ($E_{surf\text{-}NHx}$).

Nitride screening and phase diagrams

The large-scale screening of nitride candidates was completed by relaxing structures in CHGNET, employing the default simulation settings except when changing the maximum number of relaxation iterations to achieve convergence in some systems directly adapted from the Materials Project (MP) database.[2,8] Statistical results for CHGNET-DFT validation – including the Spearman correlation coefficient (R^2), mean squared error (MSE), and Kendall Tau rank correlation coefficient (τ_k) – were calculated using built-in *scipy* routines.[28] Materials systems, both directly adapted into calculations and modified via site-substitution, were extracted from MP using the Application Program Interface (API) on August 14th, 2024 or beforehand.[24] Beyond what was presented in schematic heuristics for candidate screening in Figure 2 and Figures S7-S8, convergence failure tolerances were improved from 500 to 1500 iterations for directly extracted (mostly) Al-O systems. After applying this filter, the equivalence of structures relaxed by CHGNET was evaluated by applying the Pymatgen routine "*structure_matcher*" to material subgroups possessing the same stoichiometric ratios. Following implementation of this filter, the most favorable energy with each remaining stoichiometric ratio was selected for further candidacy, though ultimately only the most favorable reduced stoichiometries from these energetically filtered systems were evaluated via phase stability analysis. Remaining materials were analyzed for theromdynamic stability.[29–31]

All energetic and thermodynamic quantities involving phase stability analysis were calculated using the "*analysis.phase_diagram*" package of Pymatgen provided by Ong *et al.*, especially its subroutine "*GrandPotentialPhaseDiagram*".[32,33] Stable phase entries were aggregated for quaternary phase diagram visualization via the "*stable_entries*" command, while quantitative phase stability results – encompassing product fractions of decomposition reactions and metastable per-atom energies above stable convex hulls – were resolved using the "*get_decomp_and_e_above_hull*" command.[32,33] Moreover, convex hull energies resolved during phase stability calculations completed for Figures 2-3, Tables S10-S11, and Figures S12-S13 were subjected to the metastability criterion detailed in Figure 2. This criterion further filtered materials that were not sufficiently metastable – or within 0.2 eV/atom of the convex hull – in at least one phase stability analysis or diagram described above, in addition to those that were not directly MP extracted. This ultimately left 46 systems remaining for CHGNET-DFT validation, which initially revealed that a single reduced stoichiometry (Al_2O_3) subjected to a more lenient convergence tolerance (1500 iterations) favored an unphysical system inconsistent with MP-estimated stability. This unphysical outcome sufficiently affected phase stability analyses, as shown via grand potential phase diagrams in Figure 2. While using all automatically filtered results made a phase diagram with seven entries, manually substituting the unphysical Al_2O_3 structure with the CHGNET energy of the MP-favored system (Al_2O_3; $R\overline{3}c$, corundum) yielded 11 stable phases.[8] This correction was applied to all further CHGNET analyses.

Lastly, refined visualizations of phase diagrams were adapted from the Python module "*python-quaternary: Quaternary Plots in Python*" by Sofiane Achour.[34]

Molecules and chemical potentials

In general, grand potential phase stability analyses modelling gas nitriding used single N-based chemical potentials (μ), which were specified to model NH_3 or N_2 molecules unless stated otherwise. Chemical potentials for atom types, represented in Grand Canonical (GC) Phase Diagram (PD) or GCPD analysis, were calculated for particular molecular contributions using the thermochemistry module of the Atomic Simulation Environment (ASE).[35] Total enthalpy ($H[T]$) terms, thermodynamically scaled to accommodate temperature (T) effects under solid oxide fuel cell (SOFC) – or N-based gas – simulated nitriding conditions (600 °C), were resolved through the following expression:[36,37]

$$H[T] = E_{pot} + E_{ZPE} + \int_0^T \left[C_{V,trans} + C_{V,rot} + C_{V,vib} + C_{V,elec}\right] dT \quad [6]$$

Here, contributions to enthalpy include the potential (or directly simulated) energy (E_{pot}) and zero-point energy (E_{ZPE}) of a molecule, as well as constant-volume heat capacity terms representing translational ($C_{V,trans}$), rotational ($C_{V,rot}$), vibrational ($C_{V,vib}$), and electronic ($C_{V,elec}$) modes of atomic motion. Similarly, total entropy ($S[T,P]$) terms that were thermodynamically scaled to treat temperature and pressure (P) effects under corresponding N-based simulated nitriding conditions (600 °C and 1 atm for NH_3, 0.5 atm for N_2), were calculated using the following equation:[36,37]

$$S[T,P] = S_{trans} + S_{rot} + S_{elec} + S_{vib} - k_B \ln\left(\frac{p}{p^0}\right) \quad [7]$$

Here, matching translational (S_{trans}), rotational (S_{rot}), vibrational (S_{vib}), and electronic (S_{elec}) contributions to total entropy were treated in tandem with changes in pressure (p) referenced to standard conditions (p^0), which were scaled by the Boltzmann constant (k_B). These enthalpy and entropy terms were used to compute corresponding Gibbs free energies ($G[T,P]$) through the defined formalism:[36,37]

$$G[T,P] \equiv H[T] - TS[T,P] \quad [8]$$

With respect to correcting simulated molecular energies to be consistent with known experimental thermodynamic results, previously resolved O_2 corrections (-1.36 eV/O_2) were adapted.[38] Corrections for NH_3, N_2, and H_2 DFT energies accounting for thermodynamic contributions were calculated referenced to standard conditions (25 °C, 1 atm) by applying Hess' Law to the following reactions:[39,40]

$$H_2(g) \rightarrow 2H^*;\ \Delta H^0 = +4.52\ eV/mol \quad [9]$$

$$N_2(g) \rightarrow 2N^*;\ \Delta H^0 = +9.79\ eV/mol \quad [10]$$

$$NH_3(g) \rightarrow 0.5N_2(g) + 1.5H_2(g);\ \Delta H^0 = -0.478\ eV/mol \quad [11]$$

By minimizing differences between experimental and simulation-resolved reaction enthalpy references (ΔH^0) across these reactions, energetic corrections (E_{corr}) for H_2, N_2, and NH_3 were respectively found to be +0.331 eV, -0.347 eV, and -0.448 eV. In particular, the N_2 correction matches that reported in former literature (-0.35 eV) very strongly.[41] Chemical potentials of each atom type were resolved from molecules by taking Gibbs free energies derived previously, and applying formerly mentioned molecular energetic corrections to them:[36–38]

$$\mu = G + E_{corr} \quad [12]$$

For gas nitriding process including H incorporation, N-based (NH_3 or N_2) and H_2 chemical potentials were applied simultaneously in stoichiometric proportions relative to chemical potentials derived previously. To develop ratios of chemical potentials modelling proportional gas flows, such as μ_{NH3}/μ_{H2}, the proportional μ contribution of H_2 was varied as a fraction of its stoichiometric value.[36]

Modular additivity functionals

In the modular additivity approach used to evaluate band gaps of ZnO under different simulation parameters, the following functionals were employed:

- Perdew-Wang 1991 (PW91, or 91)[42]
    - Here, PW91 was used to represent the Local Density Approximation (LDA) functional
- PBE revised by Zhang and Yang (revPBE, or RE)[43]
- PBE revised by Hammer (RPBE, or RP)[44]
- PBE revised for solids (PBEsol, or PS)[45]
- Armiento-Mattsson 2005 (AM05)[46–48]
- Bayesian Error Estimation Functional (BEEF, or BF)[49]

- Strongly Constrained and Appropriately Normed (SCAN)[50]
- Regularized SCAN (RSCAN)[51]
- Regularized and numerically efficient SCAN (R2SCAN)[52]
- Deorbitalized SCAN (SCANL)[53,54]
- Deorbitalized RSCAN (RSCANL)[55]
- Deorbitalized R2SCAN (R2SCANL)[56,57]

- Tao, Perdew, Staroverov, and Scuseria (TPSS)[58]
- Revised TPSS (RTPSS)[59]
- Meta Generalized Gradient Approximation functional of Sun *et al.* (MS)[60,61]
    - With regularized TPSS correlation components and exchange parameters equal to:
        - [b, c, κ] = [1.0, 0.28771, 0.29] (MS0)[60,61]
        - [b, c, κ] = [1.0, 0.18150, 0.404] (MS1)[60]
        - [b, c, κ] = [4.0, 0.14601, 0.504] (MS2)[60]

- Regularized Tao-Mo functional, version 1 (SREGTM1)[62,63]
- Regularized Tao-Mo functionals, the deorbitalized version 2 (SREGTM2L)[64]
- Orbital-free regularized-restored SCAN (OFR2)[56]
- Modified Beck-Johnson (MBJ)[65,66]
- Local MBJ (LMBJ)[67,68]

- Unscreened hybrid functional mixing Hartree-Fock with PBE correlation functional (PBE0)[4,69,70]
- Only Hartree-Fock exact exchange (HF)[71]
- PBE0 with the SCAN correlation functional (SCAN0)[4,50,69,70]
- Heyd-Scuseria-Ernzerhof (HSE) screened functionals from 2003 (HSE03)[72] and 2006 (HSE06)[73–75]
- HSE using PBEsol (HSEsol)[76]
- Range-separated hybrid functionals (RSHX) using PBE (RSHXPBE) and LDA (RSHXLDA)[77,78]
- Beck, 3-parameter, Lee-Yang Parr hybrid functional (B3LYP)[79]
    - With Vosko-Wilk-Nusair (VNW) electronic density parameter equal to:
        - 3 (B3LYP-B3)[79,80]
        - 5 (B3LYP-B5)[79,80]

Hubbard models, linear response, and modular additivity

With respect to electronic correlation, the Dudarev implementation of Hubbard *U* models was employed, with *U* parameters assigned to the respective 3*d* and 2*p* orbitals of Zn ($U_{Zn,3d}$) and O ($U_{O,2p}$) of pristine bulk ZnO.[81] These Hubbard *U* parameter values were calculated *a priori* using a linear response (LR) approach for VASP detailed in former research (LDAUTYPE = 3).[7,82] Applying LR, Hubbard $U_{Zn,3d}$ values of 4.20 ± 4.31 eV and 3.57 ± 3.65 eV were respectively calculated for the Zn 3*d* orbitals of bulk ZnO parameterized with PBE and LDA functionals. Correspondingly, Hubbard $U_{O,2p}$ results of 9.34 ± 1.07 eV and 9.12 ± 1.07 eV were respectively resolved for matching systems implementing PBE and LDA. Noticeably, all LR-calculated $U_{Zn,3d}$ had uncertainties greater than their magnitudes, such that their values are not intrinsically distinguishable from their omission or negative *U* parameters. Therefore, including these $U_{Zn,3d}$ results cannot be fully justified versus excluding them through this LR approach, supporting the decision to instead treat solely $U_{O,2p}$ in this paper in conjunction with other factors. Given LMBJ functionals solely add potential-only contributions to the exchange-correlation functionals they parameterize, such as PBE and LDA, they are not expected to change LR-derived Hubbard U values determined solely from correlation contributions to functionals.[65–68] Nevertheless, LR was completed for LMBJ-$U_{O,2p}$ models for validation purposes, achieving the same results for respective LMBJ-PBE-$U_{O,2p}$ PBE (9.34 ± 1.07 eV) and LMBJ-LDA-$U_{O,2p}$ (9.12 ± 1.07 eV) electronic structure models.

The simulation parameter additivity principle developed in this paper, which was adapted from the similar group additivity principle and related principles applied to simulation, modularly predicts simulation property values *a priori*.[7,83,84] This prediction is systematically completed by taking a known baseline property value (P_{base}) and a property value to be predicted from that baseline ($P_{predict}$), listing the differences in simulation parameters between materials systems with those property values (*param*), and then completing simulations including modular isolated subsets of those different parameters. When simulating only isolated individual parameter differences (P_i) between baseline and predicted materials systems, or neglecting covariance between larger subsets (cardinality > 1) of different parameters and other scaling relationships, the following simplified but still relatively general expression for simulation parameter additivity is produced:[84–86]

$$P_{predict} = P_{base} + \sum_{i}^{param} (P_i - P_{base}) = P_{base} + \sum_{i}^{param} \Delta P_i \quad [13]$$

Here, the contributions of individual simulation parameters to predictions referenced with respect to baseline property values are denoted as ΔP_i. For this work, this modular simulation parameter additivity principle was specifically applied to several combinations of exchange-correlation including and potential-only functionals, namely PBE (GGA), PZ (LDA), PBE-MBJ, PZ-MBJ, PBE-LMBJ, and PZ-LMBJ. For each of these functionals, band gaps (E_g) for systems applying both $U_{Zn,3d}$ and $U_{O,2p}$ Hubbard model parameters ($E_g[U_{Zn,3d};U_{O,2p}]$, or "Both U") are directly equated to baseline simulations featuring no Hubbard parameters ($E_g[NoU]$, or "No U"), as well as differential contributions from including either $U_{Zn,3d}$ ($\Delta E_g[U_{Zn,3d}] = E_g[U_{Zn,3d}] - E_g[NoU]$) or $U_{O,2p}$ ($\Delta E_g[U_{O,2p}] = E_g[U_{O,2p}] - E_g[NoU]$) parameters:

$$E_g\left[U_{Zn,3d}; U_{O,2p}\right] = E_g[NoU] + \sum_{i}^{\{U_{Zn,3d},U_{O,2p}\}} \left(E_g[i] - E_g[NoU]\right) = E_g[NoU] + \Delta E_g\left[U_{Zn,3d}\right] + \Delta E_g\left[U_{O,2p}\right] \quad [14]$$

Prediction accuracy validating this principle was quantified via Mean Squared Error (MSE) and Mean Absolute Error (MAE), comparing actual $E_g[U_{Zn,3d};U_{O,2p}]$ values with those predicted using the above expression.[87,88] Beyond predicting $E_g[U_{Zn,3d};U_{O,2p}]$ well (MSE = 0.028 eV), this expression can be applied to estimate intermediate property values – such as $E_g[U_{O,2p}]$ from $\Delta E_g[U_{O,2p}]$ – on its right-hand side. Given the relationship between adding different Hubbard U contributions is quasi-linear and proportional across each functional, such relationships were treated as modularly transferrable between each other with proportional scaling.[84,89,90] Thus, "No U" E_g and ΔE_g calculated for several functionals can heuristically estimate corresponding values for another functional after accounting for numerical scaling. Considering these premises and the experimental ZnO E_g at room temperature (E_g[expt.] = 3.37 eV),[91] PBE or PZ correlation functionals with MBJ and LMBJ potential-only functionals were estimated to strongly approach experimental E_g while modularly adding either $U_{Zn,3d}$ or $U_{O,2p}$ (E_g = 3.12-3.53 eV). Extending the modular additivity principle to search for electronic structure models most closely approximating experimental results, PBE-LMBJ-$U_{O,2p}$ was predicted to most accurately approximate experimental E_g (E_g[PBE-LMBJ-$U_{O,2p}$] = 3.34 eV).[91] Thus, adapting the simulation parameter additivity approach to modularly search for accurate electronic structure models selected simulations applying the LMBJ functional and $U_{\mathrm{O,2p}}$.[67,68]

General electronic structure and conductivity

All electronic structure related plots developed for simulations employing Hubbard models were constructed using the "electronic_structure" package within Pymatgen. In order to precisely estimate quantitative properties related to electronic structure – such as E_g – for ZnO and AZO, the number of grid points (NEDOS) used to resolve the electronic density of states (DOS) for each studied materials system was convergently tested across systems representatively. In these cases, typical NEDOS values applied to ZnO and AZO were 1501 and 2401, respectively. To precisely extract electronic structure property values from plots printed in prior experimental research – such as those from Truong *et al.* – and adapt them to current analyses, the plot digitizer *WebPlotDigitizer* designed by Ankit Rohatgi of *Automeris.io* was implemented.[92,93] Unless stated otherwise, DFT simulation parameters employed in electronic structure calculations are described in the *General Simulation* subsection of this section.

Given the complexities of electronic structure properties treated in this work, band gap (E_g) was explicitly defined as the difference between the valence band maximum (E_{VBM}) and the conduction band minimum (E_{CBM}) energies of each materials system here:[94–96]

$$E_g = E_{CBM} - E_{VBM} \quad [15]$$

For ZnO and sufficiently electronically undoped ZnO-based systems, E_{VBM} was equal to the Fermi level (E_F). When handling AZO, the effects of considering different mechanisms for charge transfer – or excitation of electrons from valence to conduction band – were more rigorously treated according to this formalism and others.[97–99] For example, the energy gap of electron excitation (E_{ex}), adapted from previous work, sums the commonly defined band gap (E_g) with a shift (ΔE_{shift}) compensating for shallow donor states. This shift references the energy gap of AZO to E_F, such that it can be more comprehensively compared with ZnO:[97,99]

$$E_{ex} = E_g + \Delta E_{shift} = E_g + (E_F - E_{CBM}) \quad [16]$$

Further, the VBM of AZO (E_{VBM}[AZO]) is subtracted from that of pristine ZnO (E_{VBM}[ZnO]) to reveal shifts in VBM versus varying impurity concentration as a property ($E_{VBM,norm}$[AZO]). Within the manuscript, this is denoted as "E-E_{ZnO}" in relation to plotted VBM series for simplicity:

$$E_{VBM,norm}[AZO] = E_{VBM}[AZO] - E_{VBM}[ZnO] \quad [17]$$

With respect to conductivity (σ) resolved using the BoltzTraP2 software package, the real space grid used throughout σ calculations was interpolated to be tenfold denser than that inputted in VASP simulations (*lpfac*=10).[100,101] To summarize calculation details relevant to topics covered in this work, start with the density of states (DOS) presented as a variable ($n(\varepsilon)$) that is a function of electronic structure band energies (ε). Over Fermi surfaces with dimensions given by wavevectors ($\boldsymbol{k}$), which are calculated from interpolated k-point grids and are correspondingly volumetrically normalized ($8\pi^3$), the energy ($\varepsilon_{b,k}$) of each sampled band (b) at each interpolated k-point (k) is enumerated via a Dirac delta function (δ). Normalized densities of bands are thereby calculated via the following formalism:[100,102,103]

$$n(\varepsilon) = \int \sum_b \delta(\varepsilon - \varepsilon_{b,\boldsymbol{k}}) \frac{d\boldsymbol{k}}{8\pi^3} \quad [18]$$

The above formalism is equated to carrier concentration (n_e) as a function of temperature (T) and the electronic component of chemical potential (μ_{ne}), which is determined by n_e but is not directly related to chemical potential from phase stability analyses (μ). The domain (E_+/E_-) over which electronic bands are symmetrically sampled relative to E_F was set in BoltzTraP2 (*energy_range*=7.5 eV, or E_+=+7.5 eV and E_-=-7.5 eV), broadly subsuming bands near E_g across ZnO-based systems.[100,101] Upon applying terms for nuclear charges (N) and the Fermi distribution function ($f^{(0)}$), the following equation is developed:[100]

$$n_e(\mu_{n_e}, T) = N - \int_{E_-}^{E_+} n(\varepsilon) f^{(0)}(\varepsilon;\ \mu_{n_e}, T) d\varepsilon \quad [19]$$

Per prior formalisms, the Fermi distribution function is calculated using the Boltzmann constant (k_B), sampled band energies (ε), and previously defined variables:[99,104,105]

$$f^{(0)}(\varepsilon;\ \mu_{n_e}, T) = \frac{1}{e^{(\varepsilon - \mu_{n_e})/k_B T} + 1} \quad [20]$$

Parameterizing the Boltzmann Transport Equation (BTE) with the Rigid Band Approximation (RBA), transport distribution tensors can be derived as a function of band (b) and wavevector (k) for conductivity tensor products ($\sigma_{\alpha\beta}(b,k)$). In the expression for this property, the cross-product of per-band and per-wavevector group velocity tensors ($\boldsymbol{v}$), which are calculated with respect to directional components (α={x,y,z}, β={x,y,z}), is scaled with respect to electron charge (e):[100–102]

$$\sigma_{\alpha\beta}(b,k) = e^2 \tau_{b,k} [\boldsymbol{v}_\alpha(b,\boldsymbol{k}) \otimes \boldsymbol{v}_\beta(b,\boldsymbol{k})] \quad [21]$$

Here, $\tau_{b,k}$ is a set of relaxation time parameters fully generalized to a per-band and per-wavevector basis. However, BoltzTraP2 and previous literature approximate this to a single parameter (*CRTA*) over all bands and wavevectors through the constant relaxation time approximation (CRTA), which is generally applied throughout this work unless otherwise stated.[100,106] Per band and wavevector domain, group velocity measures band curvature versus the derivative of band energy with respect to wavevector:[101,104]

$$v(b,k) \propto \frac{\partial \varepsilon(\boldsymbol{k})}{\partial k} \quad [22]$$

Applying all expressions derived above, the conductivity distribution ($\sigma_{\alpha\beta}(\mu_{ne}, T)$) can be calculated as a function of the n_e-based chemical potential and T. This is resolved as the product of the derivative of the Fermi distribution – taken with respect to band energy – and the conductivity tensor, which are normalized relative to cell volume (Ω):[100–102]

$$\sigma_{\alpha\beta}(\mu_{n_e}, T) = \frac{1}{\Omega} \int \sigma_{\alpha\beta} \left[-\frac{\partial f^{(0)}(\varepsilon;\ \mu_{n_e}, T)}{\partial \varepsilon} \right] d\varepsilon \quad [23]$$

Given the largest magnitudes of directional conductivity tensor components of studied ZnO-based systems existed along their diagonal entries (σ_{xx}, σ_{yy}, and σ_{zz}), the average of the diagonals of $\sigma_{\alpha\beta}$ ($[\sigma_{xx} + \sigma_{yy} + \sigma_{zz}]/3$) strongly approximated the final scalar values of σ. Over all BoltzTraP2 calculations completed here, n_e are T are inputted in tandem with electronic structures to calculate these σ. All band structure properties and σ were calculated using unit cell representations of studied ZnO-based systems.[100,101]

ZnO charge transfer quasi-reactions

In a quasi-kinetic model of electronic mobility, charge transfer of electrons from the valence band minimum (VBM) to the conduction band maximum (CBM) of an electronic structure is treated. In this quasi-reaction, the process of an electron jumping across the band gap has an activation barrier approximated as an enthalpic function of E_g (H), and a pre-factor (K_0) effectively modelling the equilibrium between electrons (n) and holes (p) during recombination.[107–109] Here, conductivity is calculated over changing temperature (T), relaxation (scattering) time parameters (τ) known from prior empirical research, and electronic carrier concentrations (n_e) that are compared with prior experimental data.[93,110,111] In surface ZnO electronic structure calculations, a constant τ of $1.18\text{x}10^{-15}$ s sufficiently approximated experimental σ-T trends within experimental uncertainty of n_e and σ.[93] Similarly, the relative values of H-inserted V_{Zn}-ZnO were resolved with a constant τ of $1\text{x}10^{-14}$ s across CRTA σ/τ domains.[106] However, $\tau_{b,k}$ are expanded beyond the simplifying CRTA approximation for bulk pristine ZnO σ calculations, as their predominant contribution to scattering is electron-phonon (e-ω) interactions and the effects of variable τ are significant.[111] When calculating σ through this approach, τ is characterized through an empirical experimental relationship with temperature and electronic carrier concentration:[102,111,112]

$$\tau = 2.53 \times 10^{-5} T^{-1} n_e^{-1/3} \quad [24]$$

For these σ calculations, variation of n_e and T versus a reference state ($n_{e,0}$, T_0) is modelled via an Arrhenius equation over a temperature differential (ΔT), using Boltzmann's constant (k_B):[107–109]

$$n_e = T^{3/2} K_0 e^{-H/kT} \propto e^{-\frac{f[E_g]}{k_B T}} \quad [25]$$

$$\ln\left(\frac{n_e}{n_{e,0}}\right) = \frac{3}{2}\ln(\Delta T) + \ln(K_0) + \left(-\frac{f[E_g]}{k_B \Delta T}\right) \propto -\left(\frac{1}{\Delta T}\right) f[E_g] \quad [26]$$

Matching experimental results, n_e vs. $1000/T$ was plotted for all studied systems to resolve linear relationships.[108,109,113] Given the function of E_g ($f[E_g]$) calculating the effective activation barriers of these processes is not known in current simulations, values of n_e inputted into BoltzTraP2 were interpolated via endpoint pairs from prior experimental σ-T trends.[93,100,109] The bulk or surface endpoints of experimental trends were quantitatively matched to each corresponding simulated conductivity σ-*T* relationship by their σ values, thereby fitting *H* from the slopes of ln(n_e) vs. -1/*T*. Using those slopes and the lowest temperature (*T*, σ) endpoint of each simulated relationship, all other (1000/*T*, n_e) values were interpolated or extrapolated under the premise that ln(n_e) vs. 1/*T* is linear.[108,109,113] These n_e results were used to calculate corresponding simulated conductivity σ-*T* relationships. Through this procedure, non-endpoint simulated σ are validated versus uncertainty in experimental *σ-T* trends, while simulated n_e determining both endpoint and non-endpoint *σ* are verified via *post hoc* comparisons with experimental n_e.[93,110]

AZO electron mobility vs. mechanism

The scattering time (equated to τ) of a quasi-reactive charge transfer mechanism can be generally expressed in terms of its effective charge (*q*), its effective mass (*m**), and its electronic mobility (μ_{e-}), and correlated with AZO Al-impurity concentration (N_i) variation accordingly:[114]

$$\mu_{e-} = \frac{q}{m^*}\tau \rightarrow \tau = \frac{m^*}{q}\mu \rightarrow \boldsymbol{\tau(N_i) \propto \mu_{e-}} \quad [27]$$

For quasi-kinetic contributions to charge mobility associated with Al impurity interactions at higher Al concentrations, corresponding electronic mobility (μ_{imp}) contributions can be expressed as:[115,116]

$$\mu_{imp} = \frac{3(\varepsilon_r\varepsilon_0)^2h^2}{Z^2(m^*)^2e^3} \times \frac{n_e}{(N_i/Z)} \times \frac{1}{F(\xi)} \rightarrow \mu_{imp}(N_i) \propto \frac{1}{Z} \times \frac{1}{N_i} \times \frac{1}{F(\xi)} \times n_e \quad [28]$$

Here, ε_0 is vacuum permittivity, ε_r is the relative dielectric constant of the studied material (7.8 for AZO), *e* is the charge of a single electron, *h* is the Planck constant, and n_e is the electron carrier concentration (varies according to previous research).[115–117] *Z* is the effective charge state of Al impurities scaled to account for interactions between impurity clusters that centralize electronic scattering. *F(ξ)* is the screening potential function characterizing the energetics of bound states during electronic excitation, such as electron-hole based interactions.[114–116] Given property-dependent τ can be calculated via interpolating and scaling known band structures, new τ_{imp} can be resolved from known τ_{imp} sharing a main scattering contribution from the proportionality relation:[100,116]

$$\boldsymbol{\tau_{imp}}(N_i) \propto \frac{\mathbf{1}}{\boldsymbol{Z}} \times \frac{\mathbf{1}}{\boldsymbol{N_i}} \times \frac{\mathbf{1}}{\boldsymbol{F(\xi)}} \times \boldsymbol{n_e} \quad [29]$$

F(ξ) is characterized using the following relationship adapted from Pisarkiewicz:[115,116,118]

$$F(\xi) = 1 + \frac{4\xi_{np}}{\xi}\left(1 - \frac{\xi_{np}}{8}\right)\ln(1+\xi) - \frac{\xi}{1+\xi} - 2\xi_{np}\left(1 - \frac{5\xi_{np}}{16}\right) \quad [30]$$

The parabolic component of the screening function (ξ) is treated according to known quantities, and newly calculated ξ values can be proportionally scaled according to changes in m^*:[115,116]

$$\xi = (3\pi^2)^{\frac{1}{3}} \times \frac{(\varepsilon_r \varepsilon_0)^2 n_e^{\frac{1}{3}}}{m^* e^2} \rightarrow \xi(N_i) \propto n_e^{1/3} \quad [31]$$

Here, the non-parabolic (*np*) character of conduction bands is modelled using the screening parameter ξ_{np}, with m_0^* being the effective mass of excited electrons at the CBM:[115–117]

$$\xi_{np} = 1 - \frac{m_0^*}{m^*} \rightarrow \xi_{np}(N_i) \propto m_0^* \quad [32]$$

Here, m_0^* can be equated to m^* by linearly interpolating the energy of excited electrons (E) relative to its respective E_{CBM} according to a band non-parabolicity parameter (C = 0.56 eV^{-1}):[115,116]

$$m^* = m_0^*\big(1 + 2C(E - E_{CBM})\big) \quad [33]$$

At higher Al-impurity concentrations, AZO band structure near E_{CBM} is sufficiently degenerate, such that E_F can be approximated using the following equation: [115,116]

$$E_F = \frac{1}{2C}\left(\sqrt{1 + 2C\left(\frac{h^2}{4\pi^2 m_0^*}\right)(3\pi^2 n_e)^{\frac{2}{3}}} - 1\right) \quad [34]$$

Thereby, m^* can be described as follows, subsequently simplifying estimation of m_0^*/m^*: [115,116]

$$m^* = m_0^*\sqrt{1 + 2C\left(\frac{h^2}{4\pi^2 m_0^*}\right)(3\pi^2 n_e)^{2/3}} \rightarrow \frac{m_0^*}{m^*} = \frac{1}{2C(E_F) + 1} \quad [35]$$

Prior experimental work estimates m^* to be equal to 0.26m_e for AZO, wherein m_e is the effective mass of an electron.[116] To resolve τ_{imp} for Al-impurity concentrations of 6.13% and 8.33%, the final value of τ in the former quasi-kinetic regime (at 4.17 Al at.%) – dominated by the Moss-Burstein effect – was first calculated. This was done using the CRTA approximation and experimentally approximated n_e, fitting constant shifts to current experimental data within the Moss-Burstein regime ($\tau_{M\text{-}B}$ = 3.48x10^{-18} s). Given the BTE is calculated with the RBA, $\tau_{M\text{-}B}$ fitting accommodates constant temperature effects on electronic structure and σ. Adapting the proportionality relationships for μ_{imp} above, τ_{imp} was calculated via scaling relative to $\tau_{M\text{-}B}$ as a reference.[100,114,116] According to former research, n_e resolved by *WebPlotDigitizer* at 4.17, 6.13, and 8.33 Al at.% (N_i) correspond to Z=1-3.[92,115]

For each scattering process characterized by an independent charge transfer mechanism, the total Hall effect associated mobility of electrons – and corresponding relaxation parameter – across quasi-kinetic regimes can be treated using Mattheissen's rule:[111,114–117]

$$\frac{1}{\tau_{total}} = \frac{1}{\tau_{e-\omega}} + \frac{1}{\tau_{M-B}} + \frac{1}{\tau_{imp}} + \cdots \qquad [36]$$

For pristine bulk ZnO materials without Al impurities, σ-T relationships varying with n_e were matched to experimental data within uncertainty, solely treating electron-phonon based contributions to electron mobility and matching relaxation parameters ($\tau_{e\text{-}\omega}$).[111] At non-zero Al impurity concentrations below the 4-6 Al at.% threshold established experimentally, τ is not known from an empirical relationship, thus it was approximated according to the CRTA as a constant fitted to experimental data.[106,112,117] As impurity concentration increased beyond this threshold, the predominant quasi-kinetic contribution was modeled to switch from the Moss-Burstein effect to impurity clustering contributions ($[\tau_{imp}]^{-1} >> [\tau_{M\text{-}B}]^{-1}$ and $[\tau_{e\text{-}\omega}]^{-1}$), such that conductivity within the high Al-impurity concentration regime was calculated using the formalisms above.[112,115–117]

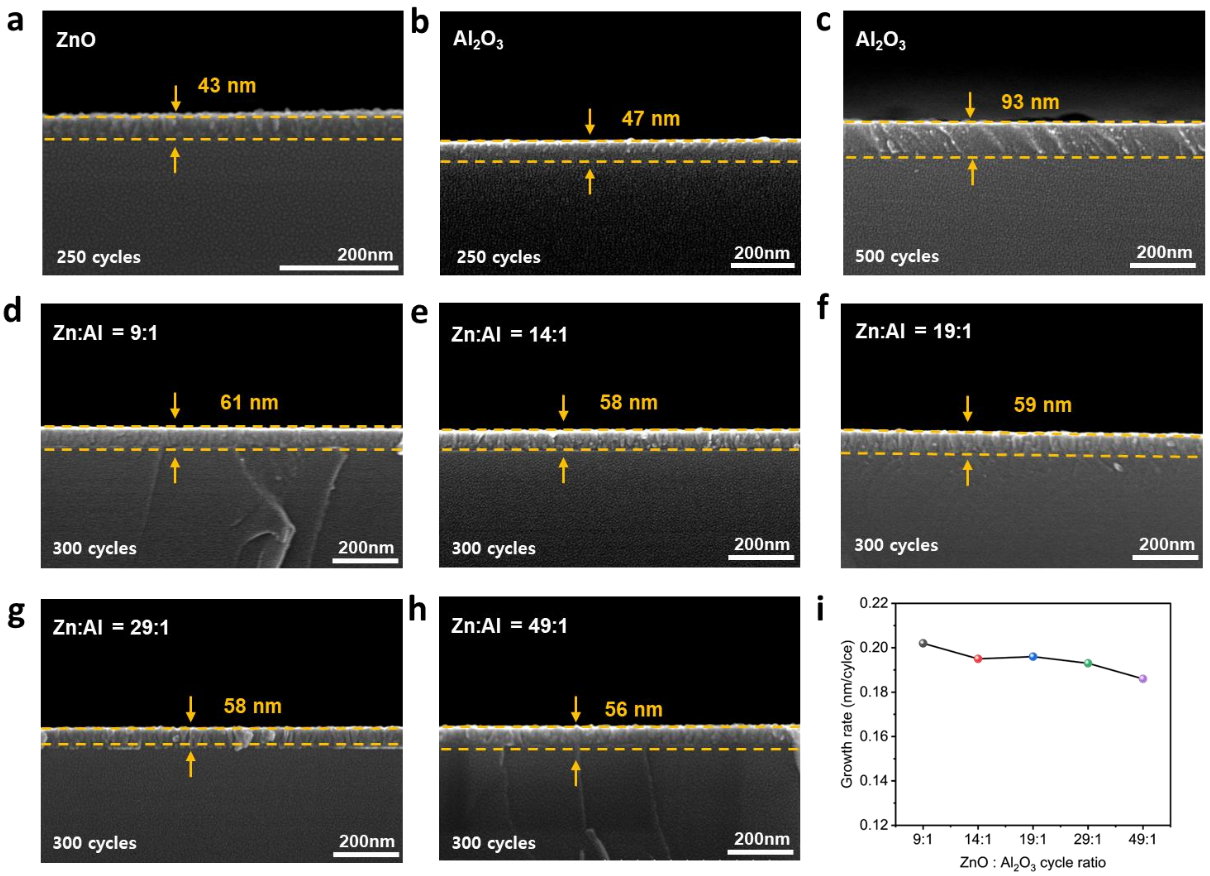

Figure S1: Scanning Electron Microscopy (SEM) images of depicting cyclical Atomic Layer Deposition (ALD) growth of unmixed **(a)** ZnO (after 250 cycles) – as well as Al_2O_3 after **(b)** 250 and **(c)** 500 cycles – on a Si wafer. Correspondingly grown ZnO:Al_2O_3 mixed composition layers assembled with respective Zn:Al ratios of **(d)** 9:1, **(e)** 14:1, **(f)** 19:1, **(g)** 29:1, and **(h)** 49:1. **(i)** Layer growth rate per cycle (GPC) plotted versus Zn:Al_2O_3 ratio. The thicknesses of all grown layers pictured are marked on their respective images (golden text), and the domains occupied by those layers are demarcated accordingly (golden dotted lines and arrows). The total number of ALD growth cycles (lower left, white text), ZnO:Al_2O_3 compositional ratios applied during ALD growth (upper left, white text), and SEM scale bars (lower right, white text) for each system are listed in each image.

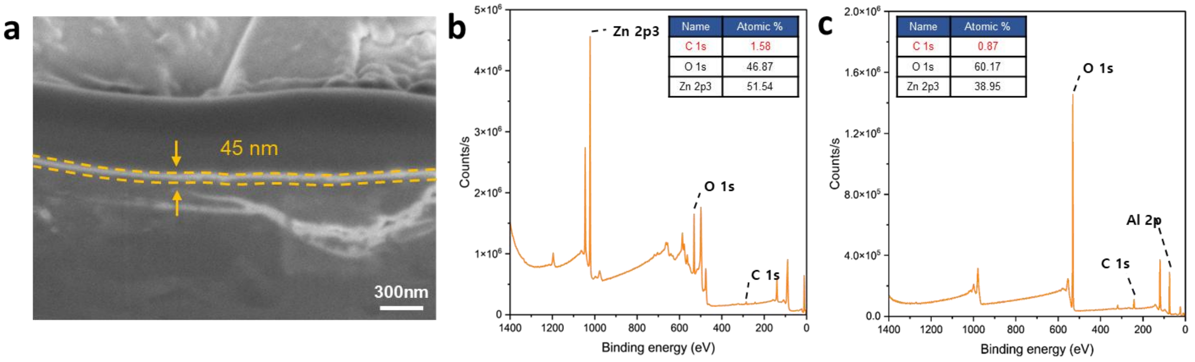

Name	Atomic %
C 1s	1.58
O 1s	46.87
Zn 2p3	51.54

Name	Atomic %
C 1s	0.87
O 1s	60.17
Zn 2p3	38.95

Figure S2: Focused Ion Beam (FIB) SEM image of **(a)** 460FC steel separators growing AZO coatings (Zn:Al = 14:1) ALD cycle ratios (scale bars: 300 nm). Grown layer thicknesses are marked on respective images (golden text, dotted lines, and arrows). X-ray Photoelectron Spectroscopy (XPS) spectra and corresponding compositional analyses for unmixed **(b)** ZnO and **(c)** Al_2O_3 systems (250 ALD cycles) on Si wafers, denoting peaks that are attributed to O, Zn, Al, and trace elemental C binding energies.

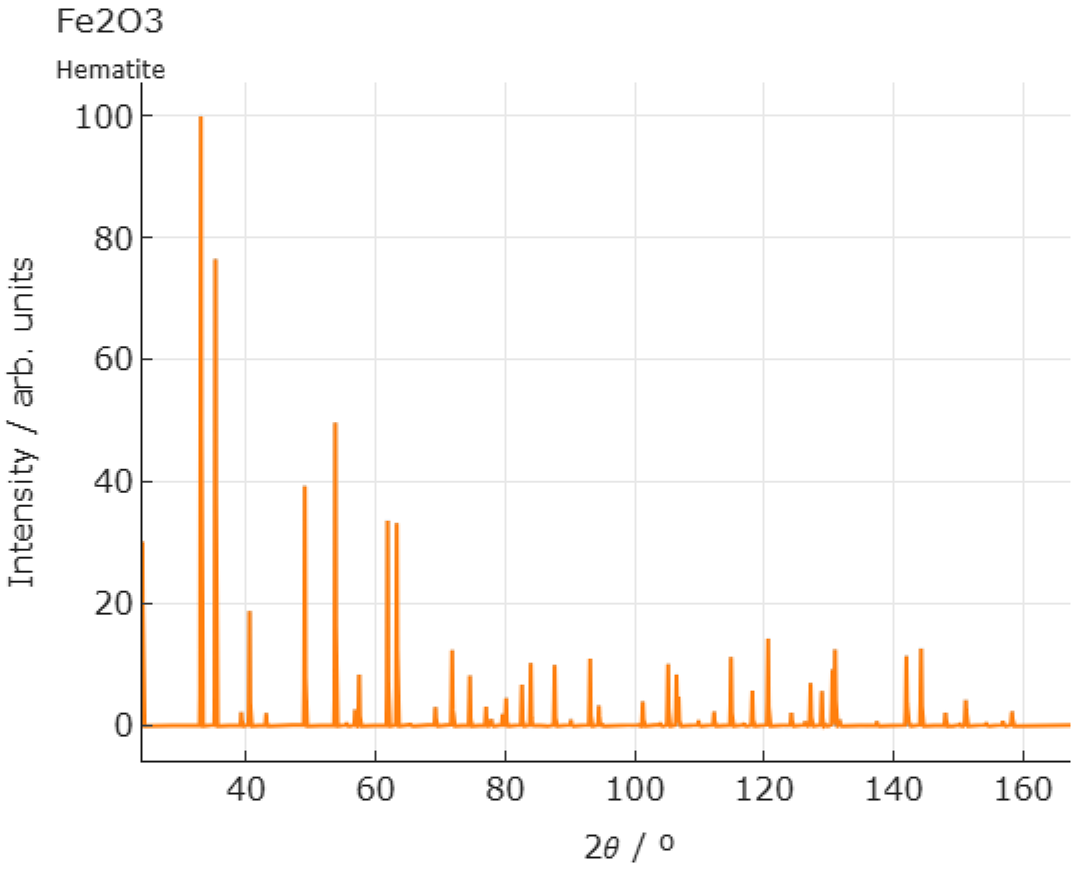

Figure S3: X-ray Diffraction (XRD) reference spectrum generated for α-Fe_2O_3 (hematite, mp-19770) from simulated data via MP (Pymatgen),[8,119] applying CuKα (1.542 Å) radiation, a shape factor of 0.94, a Gaussian peak profile, and a crystallite size of 1 nm. In the current analysis, peak ratio proportions were assessed for only the first and second highest intensity peaks respectively located at 33.00° and 35.25°, which are correspondingly indexed to $(10\bar{1}4)$ or (104) and $(11\bar{2}0)$ or (110) for α-Fe_2O_3.

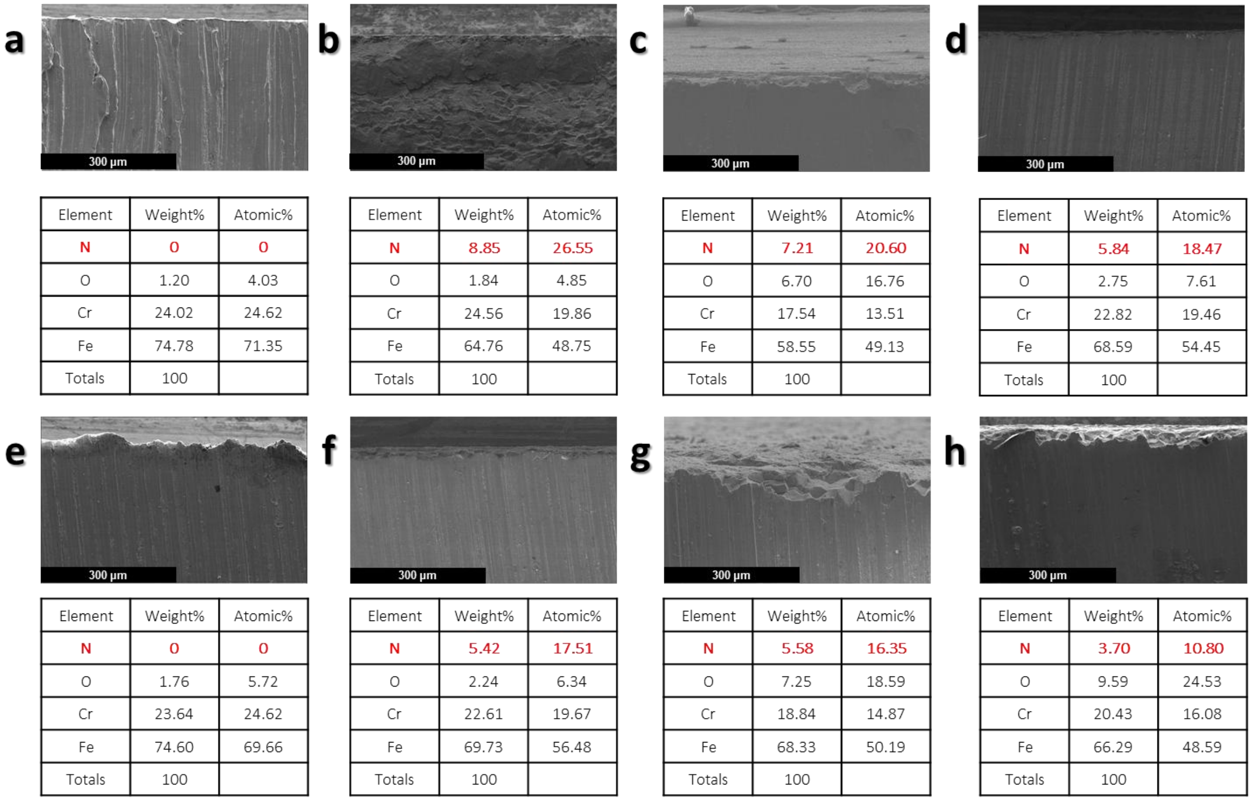

a

Element	Weight%	Atomic%
N	0	0
O	1.20	4.03
Cr	24.02	24.62
Fe	74.78	71.35
Totals	100	

b

Element	Weight%	Atomic%
N	8.85	26.55
O	1.84	4.85
Cr	24.56	19.86
Fe	64.76	48.75
Totals	100	

c

Element	Weight%	Atomic%
N	7.21	20.60
O	6.70	16.76
Cr	17.54	13.51
Fe	58.55	49.13
Totals	100	

d

Element	Weight%	Atomic%
N	5.84	18.47
O	2.75	7.61
Cr	22.82	19.46
Fe	68.59	54.45
Totals	100	

e

Element	Weight%	Atomic%
N	0	0
O	1.76	5.72
Cr	23.64	24.62
Fe	74.60	69.66
Totals	100	

f

Element	Weight%	Atomic%
N	5.42	17.51
O	2.24	6.34
Cr	22.61	19.67
Fe	69.73	56.48
Totals	100	

g

Element	Weight%	Atomic%
N	5.58	16.35
O	7.25	18.59
Cr	18.84	14.87
Fe	68.33	50.19
Totals	100	

h

Element	Weight%	Atomic%
N	3.70	10.80
O	9.59	24.53
Cr	20.43	16.08
Fe	66.29	48.59
Totals	100	

Figure S4: Combined cross-sectional SEM and Energy Dispersive X-ray (EDX) spectroscopy analysis respectively visualizing Crofer 22 APU separators (Zn:Al = 14:1) under varied conditions and measuring their elemental compositions by weight and atomic fractions (%). Nitrided (N) Steel (Fe-Cr-O) morphologies and components are measured for separators without AZO coatings (“bare”) **(a)** before and **(b)** after 60 h of NH_3 exposure, as well as for AZO-coated separators after **(c)** 24 and **(d)** 60 h of NH_3 exposure. Corresponding 460FC results study “bare” separator **(e)** before and **(f)** after NH_3 exposure for 60 h, with complementary AZO-coated results after **(g)** 24 h and **(h)** 60 h of NH_3 exposure. Note that N is fixed at 0 in “bare” systems before nitriding, or (a) and (e), such that all other elemental components are normalized based on this setting (scale bars: 300 nm).

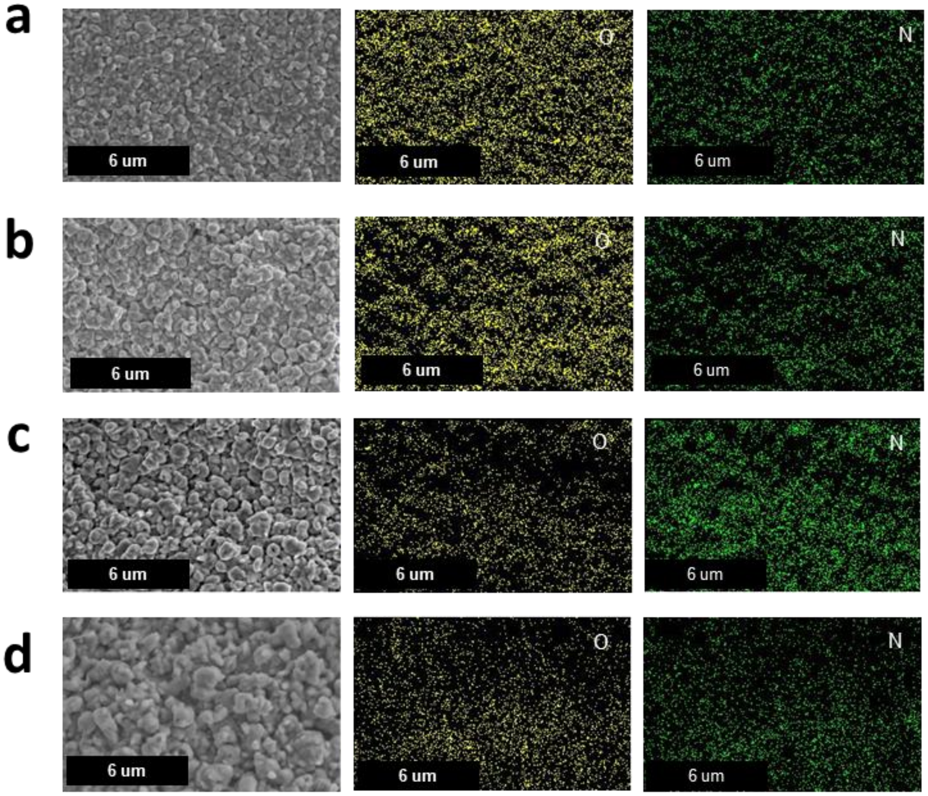

Figure S5: SEM-EDX images visualizing surfaces exposed to NH_3 for 60 h (leftward panels, scale bars: 6 μm) – as well as corresponding O (golden spots, middle panels) and N (green spots, rightward panels) EDX elemental mappings – for **(a)** Crofer 22 APU and **(b)** 460FC steel separators without AZO coatings (“bare”). Complementary results with AZO coatings are depicted for **(c)** Crofer 22 APU and **(d)** 460FC steel separators.

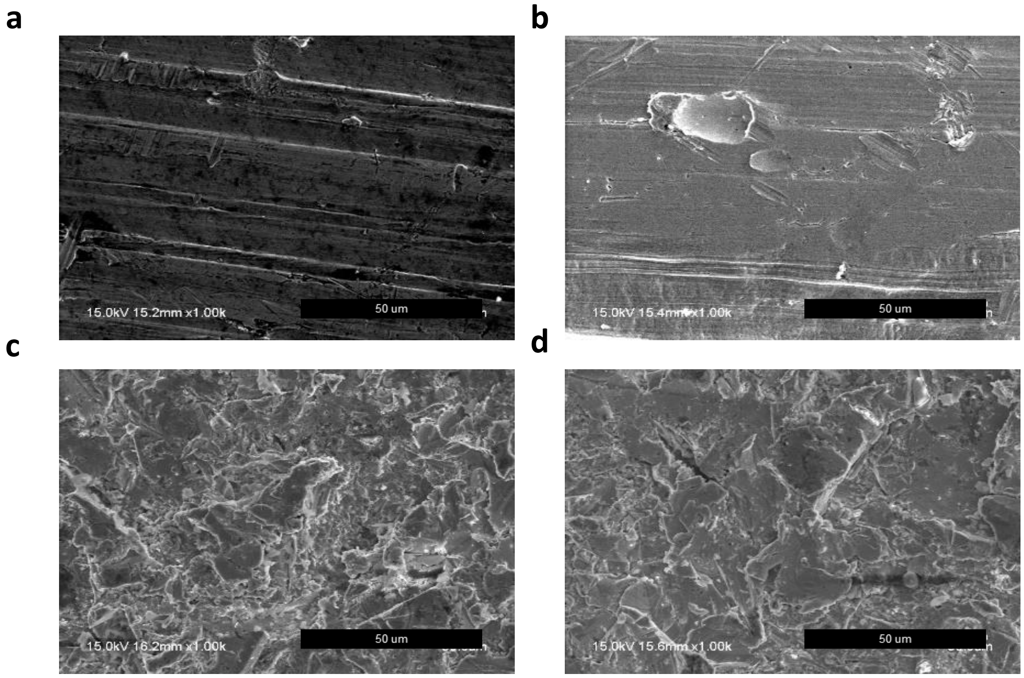

Figure S6: SEM images of **(a)** bare (no coating) Crofer 22 APU and **(b)** AZO-coated result, both before being subjected to NH_3 for 24 h. **(c)** SEM images of bare (no coating) 460FC and **(d)** AZO-coated result, similarly before 24h of NH_3 exposure.

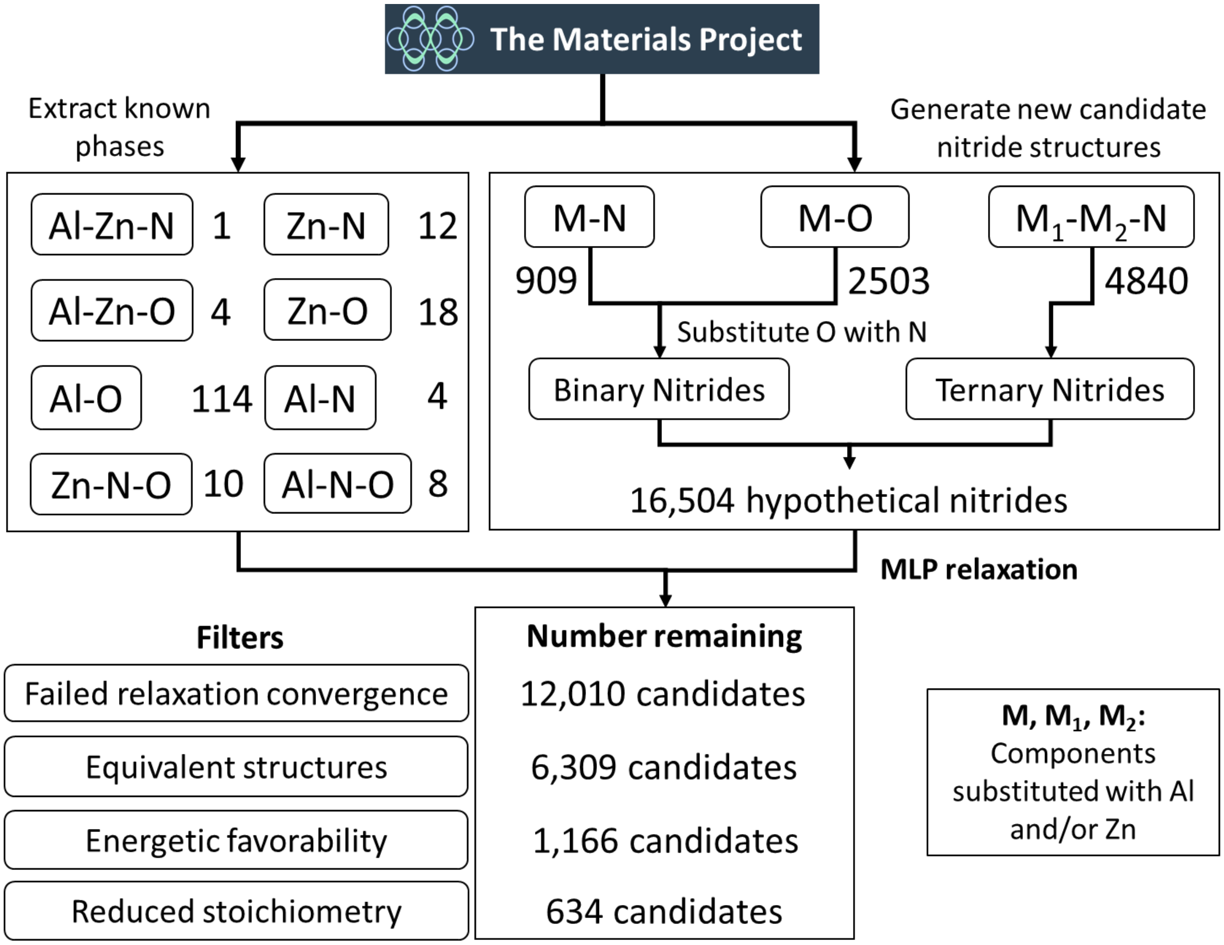

Figure S7: Schematic detailing several components of protocol, including MP extraction of known Al-Zn-O-N based phases, nitride candidate generation from templates, and candidate filtering after relaxation of nitrides using a MLP (CHGNET). Enumerations of known phases extracted from MP consisting of particular subsets of the Al-Zn-O-N phase space are listed, in addition to the numbers of binary nitride (M-N), binary oxide (M-O), and ternary nitride (M_1-M_2-N) templates adapted from MP searching. Over all binary substituted templates, any component (M; typically metal) of binary or ternary systems that was not its searched N or O component was substituted with Al in one set of relaxed systems, and Zn within another. Binary oxides had their O atoms additionally substituted with N. Ternary nitrides featured two non-N components (M_1, M_2), which were substituted with Al and Zn in alternating orders across two separate sets of systems. After MLP relaxation of all structures, several filters were applied to remove candidate phases, including structures that failed to relax within CHGNET's default convergence tolerance, and those that were found to be equivalent after relaxation according to Pymatgen's *StructureMatcher* routine. Additional criteria included removal of systems with less favorable per-atom energies than other candidates per unique unit cell composition, as well as corresponding less favorable structures per reduced stoichiometry. The numbers of candidates remaining after each filter was applied sequentially are listed accordingly.

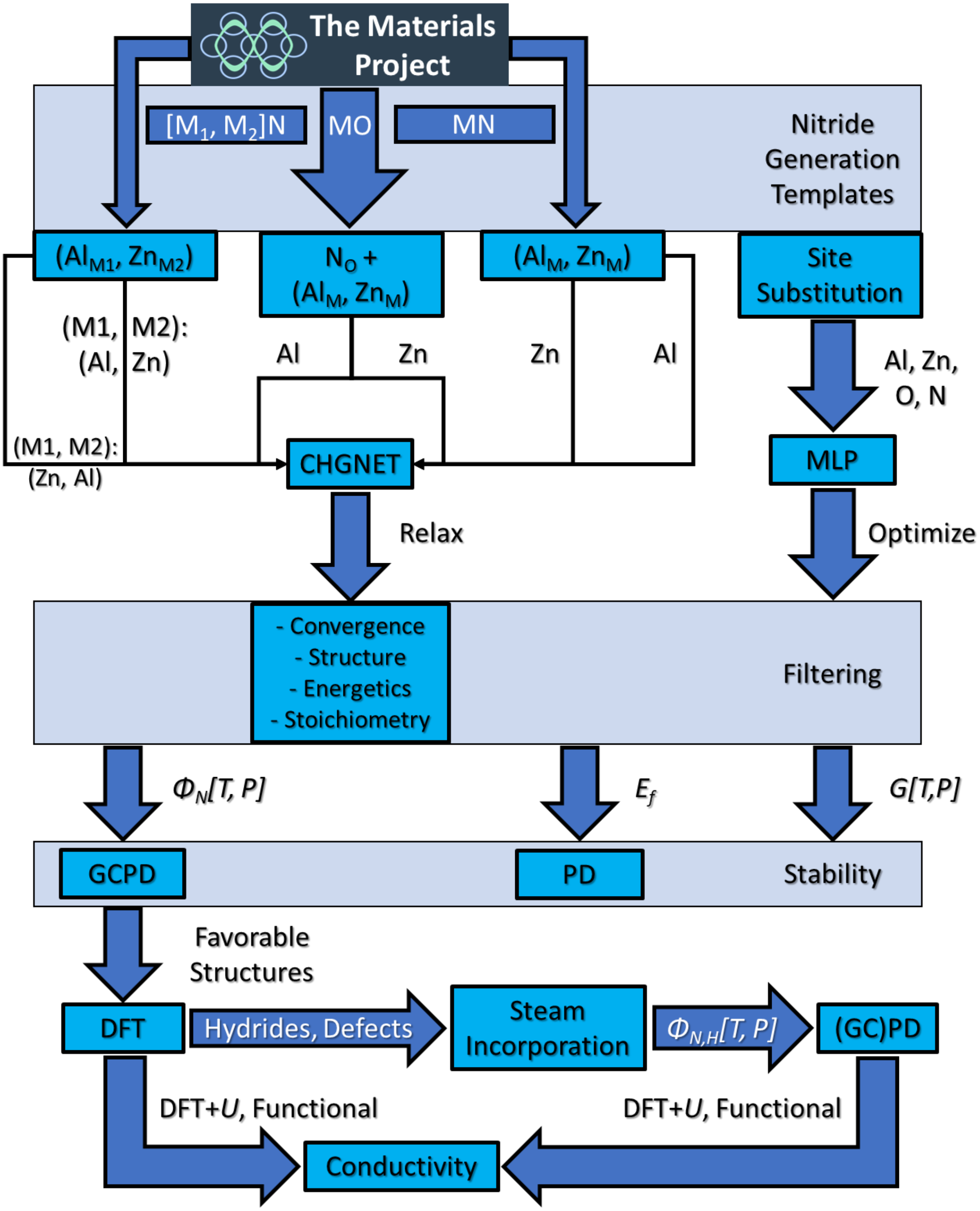
The Materials Project
$[M_1, M_2]N$
MO
MN
Nitride Generation Templates
(Al_{M1}, Zn_{M2})
N_O + (Al_M, Zn_M)
(Al_M, Zn_M)
Site Substitution
(M1, M2): (Al, Zn)
(M1, M2): (Zn, Al)
Al
Zn
Zn
Al
Al, Zn, O, N
CHGNET
MLP
Relax
Optimize
- Convergence
- Structure
- Energetics
- Stoichiometry
Filtering
$\Phi_N[T, P]$
E_f
$G[T,P]$
GCPD
PD
Stability
Favorable Structures
DFT
Hydrides, Defects
Steam Incorporation
$\Phi_{N,H}[T, P]$
(GC)PD
DFT+U, Functional
DFT+U, Functional
Conductivity

Figure S8

Figure S8: Schematic overview of whole workflow evaluating site-substituted Al-Zn-O-N based structural configurations, which outputs thermodynamically favorable phases relative to *G[T,P]* for further conductivity and hydride-based analyses. First, specific modules for generating stoichiometrically generalized nitrides from site substitution of binary nitride (MN), binary oxide (MO), and ternary nitride ([M_1, M_2]N) templates are described via Kröger-Vink notation (see Figure S7 for details). After structural optimization (relaxation) via a MLP (CHGNET) and subsequent filtering of candidates using additional criteria (Figure S7), E_f are calculated to develop PDs, which are further combined with grand canonical potentials for N-based molecules ($\Phi_N[T,P]$) at given *T* and *P* to produce GCPDs. Remaining stable structures resulting from candidate selection are validated via DFT results (Figure S7), and are subsequently applied to conductivity and hydride defect formation analyses of ZnO and AZO. DFT ZnO/AZO outcomes are parameterized with various combinations of Hubbard U and functional to determine what resolves electronic structure and conductivity most accurately, while the formation of different hydride defects is tested for favorability on related systems to evaluate the effects of steam incorporation. N and H based molecular grand potentials ($\Phi_{N,H}[T,P]$) from GCPDs are employed to evaluate hydride defect thermodynamic favorability, while conductivity analyses are repeated on resulting preferred hydride structures.

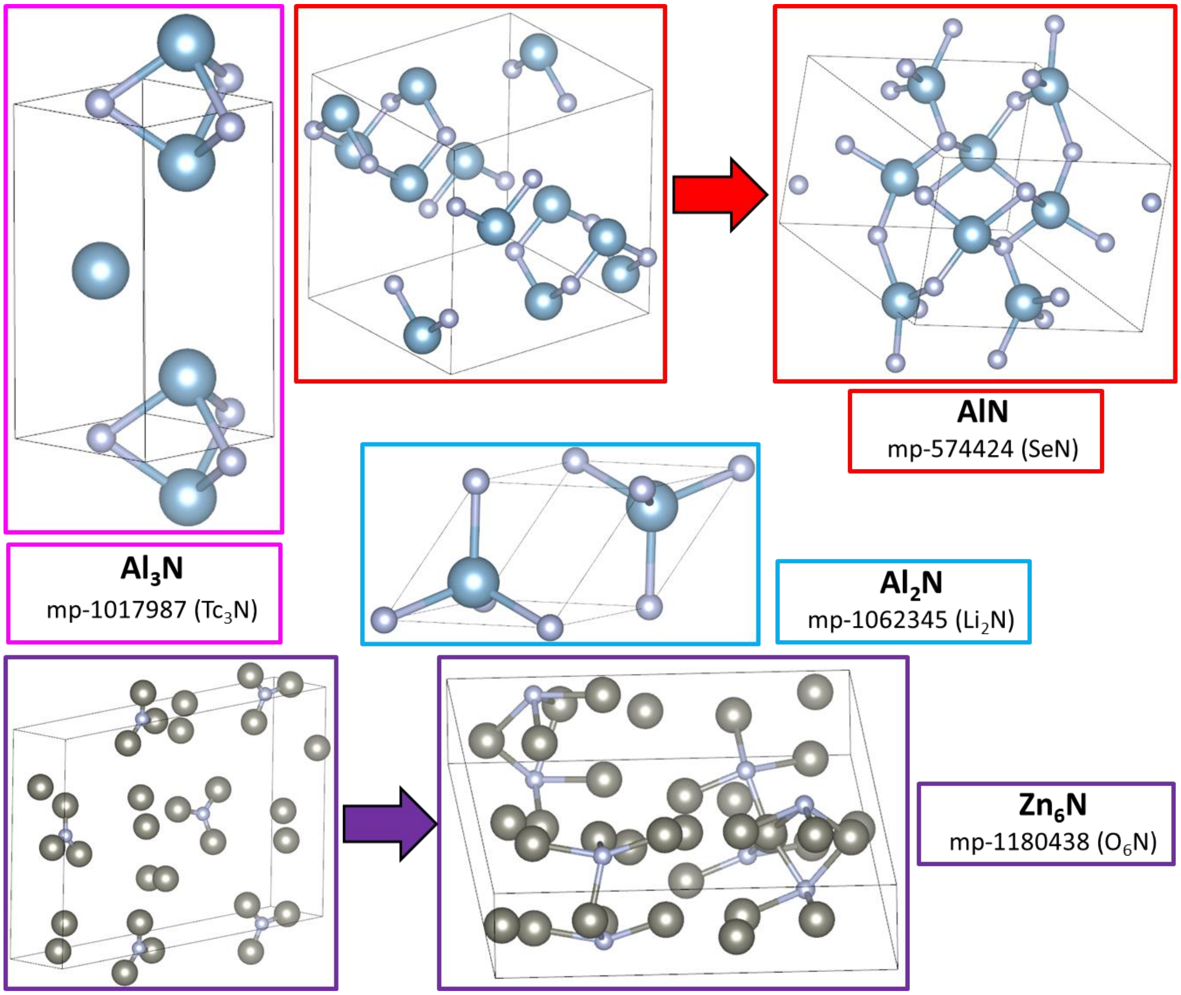

Figure S9: Templated structures generated by nitride screening procedure, which were stable – or sufficiently favorable metastable ($\leq$ 0.2 eV/atom) – phases in CHGNET PDs that were adapted to DFT validation. Bolded compositions were developed by this procedure, while MP material identification numbers (MPIDs) & systems denoted by parentheses represent the structures from which nitrides were generated. Arrows connect the initial (leftward) and final (rightward) configurations of structures that were significantly changed during CHGNET relaxation, implying that they would less likely be resolved as stable similar phases in DFT.

a

Composition	MPID
Al	mp-134
Zn	mp-79
N_2	mp-154
O_2	mp-723285
AlN_3O_{18}	mp-1204227
ZnN_2O_6	mp-772617
ZnO	mp-2133
$Al_1Zn_{53}O_{54}$	mp-2133 (ZnO)
Al_2ZnO_4	mp-2908
Al_2O_3	mp-1244994
Zn_6N	mp-1180438
Al_2Zn	mp-1206713
Al_3N	mp-1017987

b

Composition	MPID
Al	mp-134
Zn	mp-79
N_2	mp-154
O_2	mp-723285
AlN_3O_{18}	mp-1204227
ZnN_2O_6	mp-772617
ZnO	mp-2133
$Al_1Zn_{53}O_{54}$	mp-2133 (ZnO)
Al_2ZnO_4	mp-2908
Al_5O_8	mp-1182893
$Al_{11}NO_{15}$	mp-675682
$Al_{10}ZnO_{16}$	mp-760795
Al_2O_3	mp-1143
Zn_6N	mp-1180438
$Al_{38}O_{21}$	mp-1245113
Al_2O	mp-1245215
Al_2Zn	mp-1206713
Al_3N	mp-1206713

c

Composition	MPID
Al	mp-134
Zn	mp-79
N_2	mp-154
O_2	mp-723285
AlN_3O_{18}	mp-1204227
ZnN_2O_6	mp-772617
ZnO	mp-2133
Al_2ZnO_4	mp-2908
Al_5O_8	mp-1182893
$Al_{10}ZnO_{16}$	mp-760795
Al_2O_3	mp-1143
$Al_{11}NO_{15}$	mp-675682
Zn_6N	mp-1180438
$Al_{38}O_{21}$	mp-1245113
Al_2O	mp-1245215
Al_2Zn	mp-1206713
Al_3N	mp-1017987

d

Composition	MPID
Al	mp-134
O_2	mp-723285
H_2	mp-730101
Zn_6N	mp-1180438
Al_5O_8	mp-1182893
Al_2O_3	mp-1143
$Al_{10}Zn_1O_{16}$	mp-760795
Al_2ZnO_4	mp-2908
ZnO	mp-2133
$Al_{38}O_{21}$	mp-1245113
Al_2O	mp-1245215

e

Composition	MPID
O_2	mp-723285
H_2	mp-730101
Al_3N	mp-1017987
Zn_6N	mp-1180438
AlN_3O_{18}	mp-1204227
Al_5O_8	mp-1182893
$Al_{11}NO_{15}$	mp-675682

f

Composition	MPID
H_2	mp-730101
Al_5O_8	mp-1182893
Zn_6N	mp-1180438
$Al_{10}Zn_1O_{16}$	mp-760795

g

Composition	MPID
H_2	mp-730101
Al_5O_8	mp-1182893
Zn_6N	mp-1180438

Table S10

Table S10: Stable products of phase diagrams developed via CHGNET results under standard ("inert") conditions **(a)** without and **(b)** with corrections applied for Al_2O_3 energetics, while including AZO systems in stability analyses as dilute as $Al_1Zn_{53}O_{54}$. **(c)** PD resolved while reducing the AZO dilution limit to $Al_1Zn_{47}O_{48}$ and accounting for Al_2O_3 energetic corrections, as explained in (b). Reduced stoichiometric compositions (leftward columns) and corresponding MPIDs from the MP database (rightward columns) identify stable products, with AZO being adapted from corresponding ZnO structures on MP. Corresponding stable products of GCPDs developed via CHGNET results under simulated SOFC conditions (600 °C, 1 atm) using solely **(d)** NH_3 and **(e)** ½N_2 molecular chemical potentials, as well as corresponding **(f)** NH_3 and **(g)** ½N_2 potentials paired with molecular ½O_2 potentials. These stability analyses test AZO systems as dilute as $Al_1Zn_{53}O_{54}$, and employ 50/50 (mol. %) gas compositions in all mixtures (f, g). Pink highlighted rows indicate vertices of calculated three or four component phase diagrams.

a

Composition	MPID
Al	mp-134
Zn	mp-79
N_2	mp-154
O_2	mp-723285
ZnN_2O_6	mp-772617
ZnO	mp-2133
Al_2ZnO_4	mp-2908
Al_2O_3	mp-1143
AlN	mp-661

b

Composition	MPID
Al	mp-134
Zn	mp-79
N_2	mp-154
O_2	mp-723285
ZnN_2O_6	mp-772617
ZnO	mp-2133
$Al_1Zn_{95}O_{96}$	mp-2133 (ZnO)
Al_2ZnO_4	mp-2908
Al_2O_3	mp-1143
AlN	mp-661

c

Composition	MPID
Al	mp-134
Zn	mp-79
O_2	mp-723285
H_2	mp-730101
Al_2O_3	mp-1143
Al_2ZnO_4	mp-2908
ZnO	mp-2133
$Al_1Zn_{95}O_{96}$	mp-2133 (ZnO)

d

Composition	MPID
AlN	mp-661
Zn	mp-79
O_2	mp-723285
H_2	mp-730101
ZnN_2O_6	mp-772617
Al_2O_3	mp-1143
Al_2ZnO_4	mp-2908
ZnO	mp-2133
$Al_1Zn_{95}O_{96}$	mp-2133 (ZnO)

e

Composition	MPID
Al	mp-134
Zn	mp-79
N_2	mp-154
O_2	mp-723285
ZnN_2O_6	mp-772617
ZnO	mp-2133
Al_2ZnO_4	mp-2908
Al_2O_3	mp-1143
Zn(0001)-NH_2	mp-79
AlN	mp-661

f

Composition	MPID
Al	mp-134
Zn	mp-79
N_2	mp-154
O_2	mp-723285
ZnN_2O_6	mp-772617
ZnO	mp-2133
$Al_1Zn_{95}O_{96}$	mp-2133 (ZnO)
Al_2ZnO_4	mp-2908
Al_2O_3	mp-1143
Zn(0001)-NH_2	mp-79
AlN	mp-661

g

Composition	MPID
Al	mp-134
O_2	mp-723285
Zn(0001)-NH	mp-79
Al_2O_3	mp-1143

Table S11

Table S11: Stable products developed with DFT results under standard (“inert”) conditions, featuring AZO dilution limits of **(a)** $Al_1Zn_{53}O_{54}$ and **(b)** $Al_1Zn_{95}O_{96}$. Matching GCPD outcomes achieved with DFT under SOFC operating conditions and an AZO dilution limit of $Al_1Zn_{95}O_{96}$, applying **(c)** NH_3 and **(d)** N_2 molecular chemical potentials. Corresponding stable phases developed with DFT results from (a-d), while including Zn and ZnO surface model results shown in Figure 3d and Figure S13. Calculations were completed under standard (“inert”) conditions, featuring AZO dilution limits of **(e)** $Al_1Zn_{53}O_{54}$ and **(f)** $Al_1Zn_{95}O_{96}$. A matching GCPD outcome achieved with DFT under SOFC operating conditions, and an AZO dilution limit of $Al_1Zn_{95}O_{96}$, applies **(g)** NH_3 and H_2 molecular chemical potentials simultaneously. Reduced stoichiometric compositions (leftward columns) and corresponding MPIDs from the MP database (rightward columns) identify stable products, with AZO being adapted from corresponding ZnO structures on MP. Pink highlighted rows indicate vertices of calculated three or four component phase diagrams.

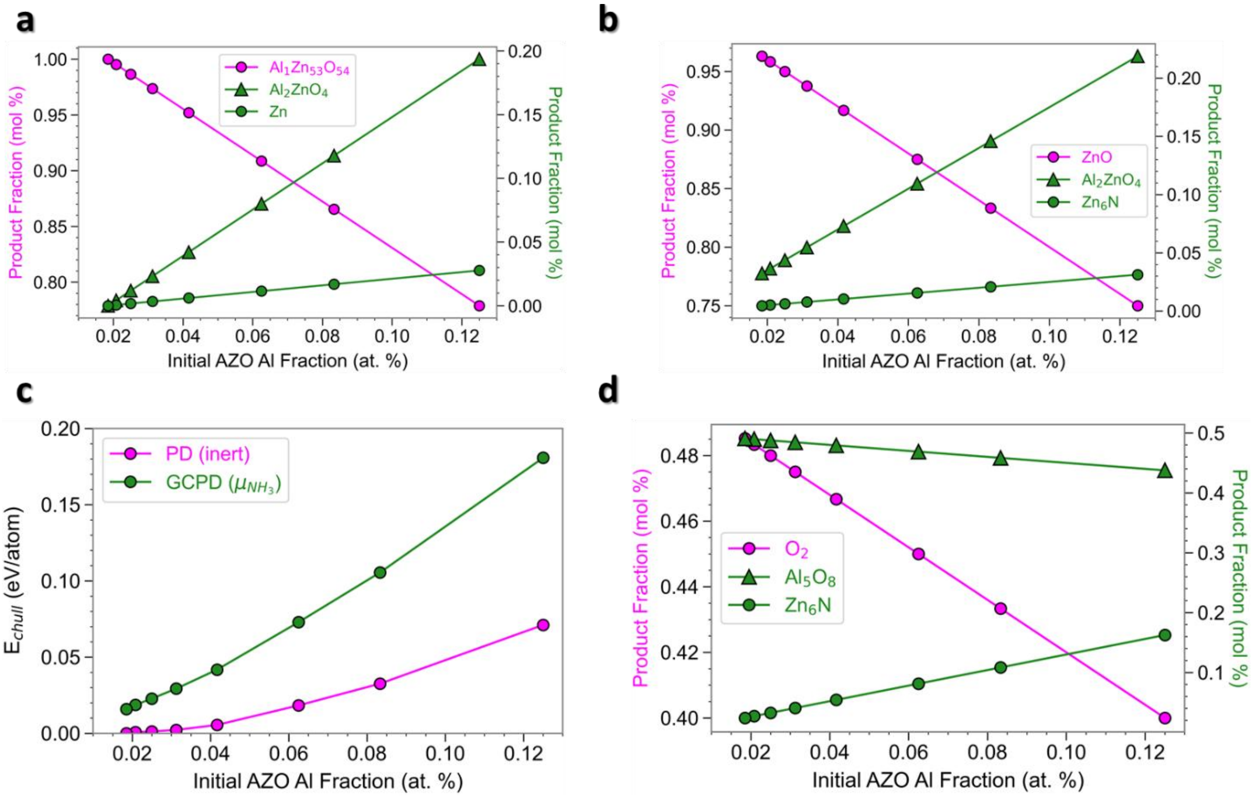

Figure S12: CHGNET-resolved products of decomposing pristine bulk AZO, which is initially composed of varied Al dopant fractions, under **(a)** standard (PD, "inert") and **(b)** SOFC (GCPD, NH_3 chemical potential) operating conditions. **(c)** Energies above convex hull of AZO (E_{chull}) in PD and GCPD stability analyses, corresponding to favorability plotted in (a) and (b). **(d)** Final product GCPD concentration profile achieved with a N_2, rather than NH_3 (Table S10), chemical potential under SOFC operating conditions.

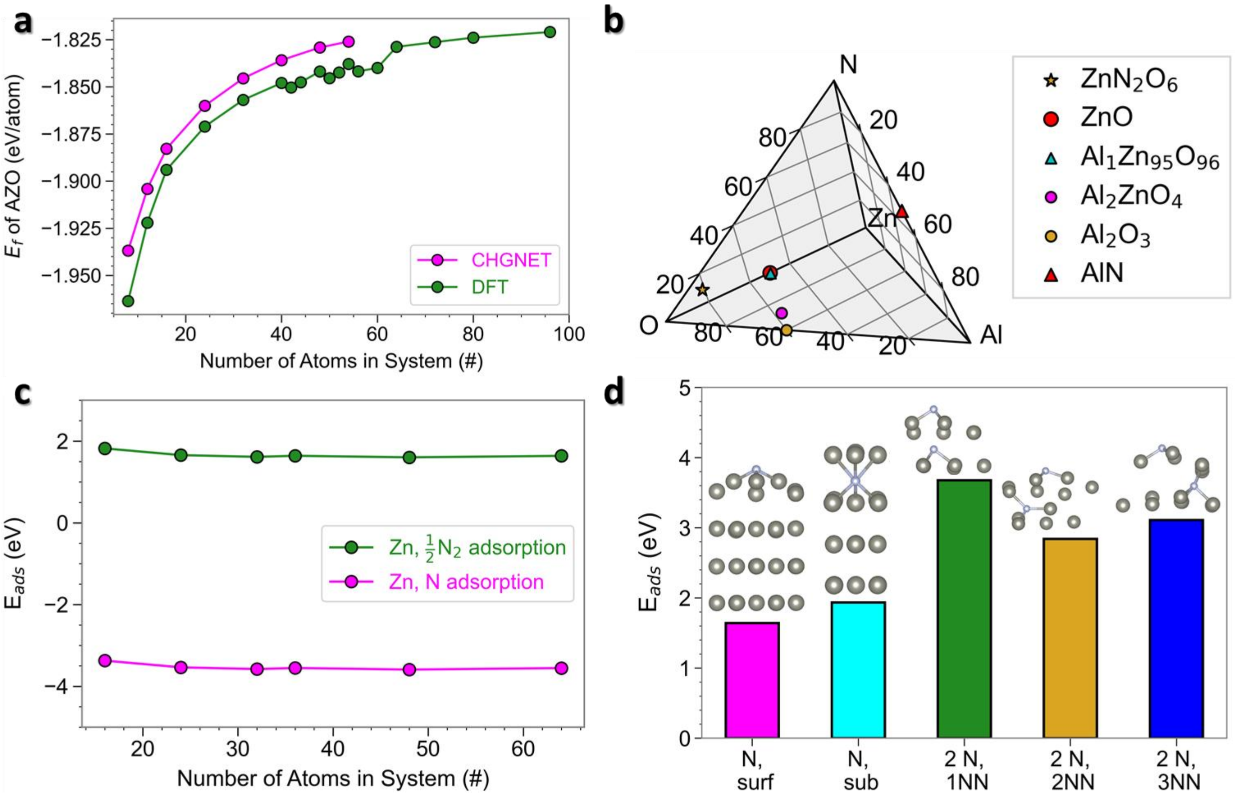

Figure S13: (a) Convergence of AZO formation energy (E_f of AZO) with the numbers of atoms in simulated, as shown for CHGNET and DFT results. **(b)** Al-Zn-N-O phase diagram calculated from DFT bulk structures under standard conditions, denoting stable phases with uniquely colored and shaped markers in correspondence with Figure 3a. **(c)** E_{ads} for single N atoms to Zn(0001) surfaces versus simulated cell size, calculated using atomic N and ½N_2 molecular chemical potentials. **(d)** Adsorption energies of single N ("N") to Zn(0001) surfaces ("surf") and subsurfaces ("sub"), matched with corresponding E_{ads} for various configurations of two N ("2N"). Each "2N" system adsorbs one N to a surface site and another to a subsurface site, depicting systems that place surface N one ("1NN"), two ("2NN"), or three nearest neighbor ("3NN") distances away from corresponding subsurface N relative to interfacial dimensions (or excluding distance perpendicular to vacuum). Atomic models for each system are placed above their respective bar graph series, while all E_{ads} are referenced with respect to the ½N_2 chemical potential.

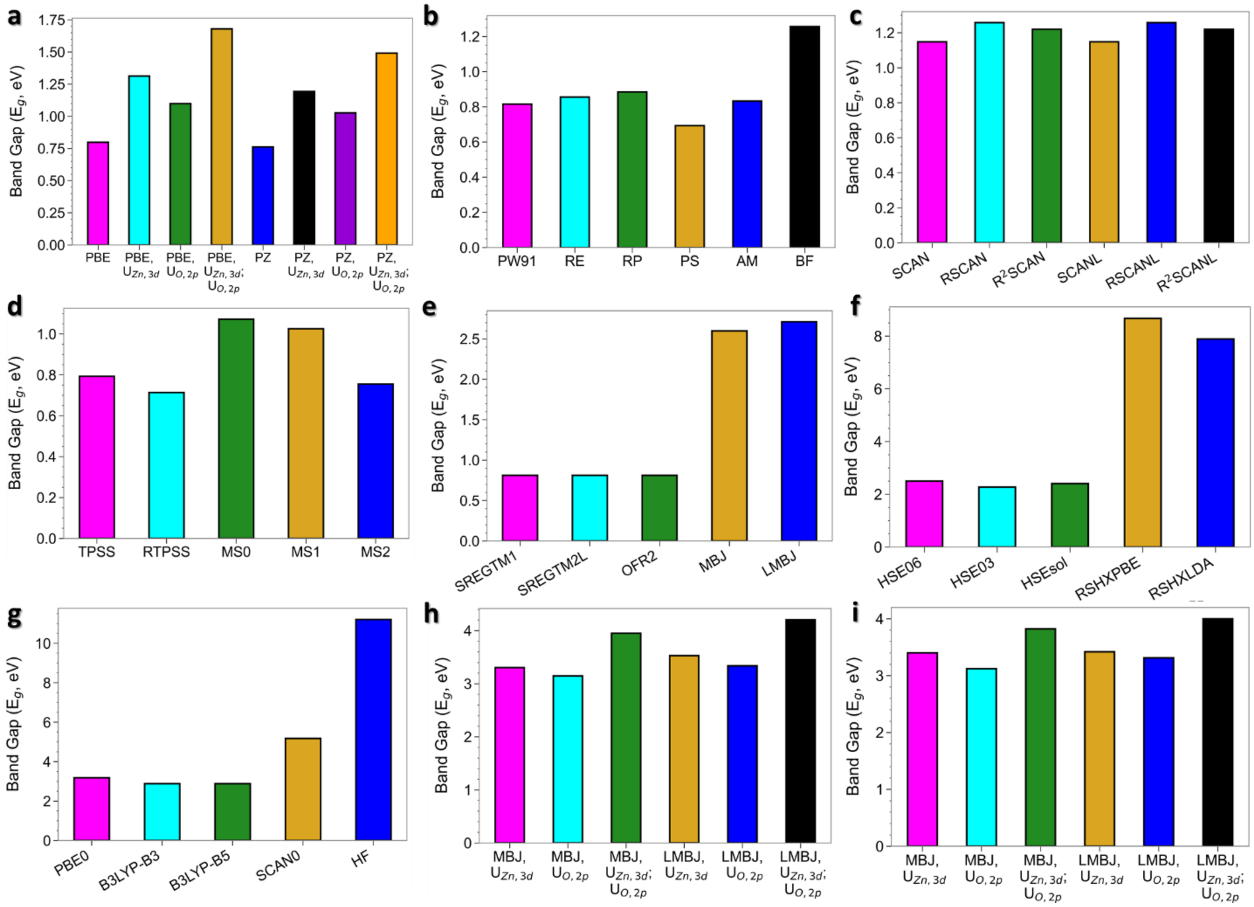

Figure S14: (a) DFT-simulated bulk ZnO E_g achieved using PBE or PZ functionals, resolved with or without Hubbard models. Hubbard models are calculated via linear response with respective functionals, including $U_{Zn,3d}$ (PBE: 4.20 eV, PZ: 3.57 eV), $U_{O,2p}$ (PBE: 9.34 eV, PZ: 9.12 eV), or both parameters ($U_{Zn,3d}$;$U_{O,2p}$). Overall, PBE and PZ E_g produce consistent trends over different Hubbard models per functional, as their ΔE_g additively relate electronic structure models applying no and individual Hubbard parameters to those applying both U. Omitting Hubbard models, E_g of a broad set of **(b)** PBE-GGA based functionals are evaluated, in addition to **(c)** SCAN based, **(d)** Tao-Perdew based, and **(e)** Tao-Mo based meta-GGA functionals. Hybrid functionals that **(f)** employ or **(g)** omit HSE-screening are also tested, with PBE0 (3.18 eV) moderately resembling experimental E_g (3.37 eV).[91] However, ZnO electronic structure models combining MBJ and LMBJ potential-only functionals with various Hubbard parameterizations were tested using **(h)** PBE and **(i)** PZ correlation functionals. U calculated via MBJ and LMBJ functionals were equal to those achieved with PBE and PZ functionals, thus equivalent Hubbard models were employed across these systems. Unless otherwise noted, functionals providing potential-only or other partial components to functional calculations, such as MBJ/LMBJ (e, h) and RSHXPBE (f), are supplemented by PBE correlation functionals.

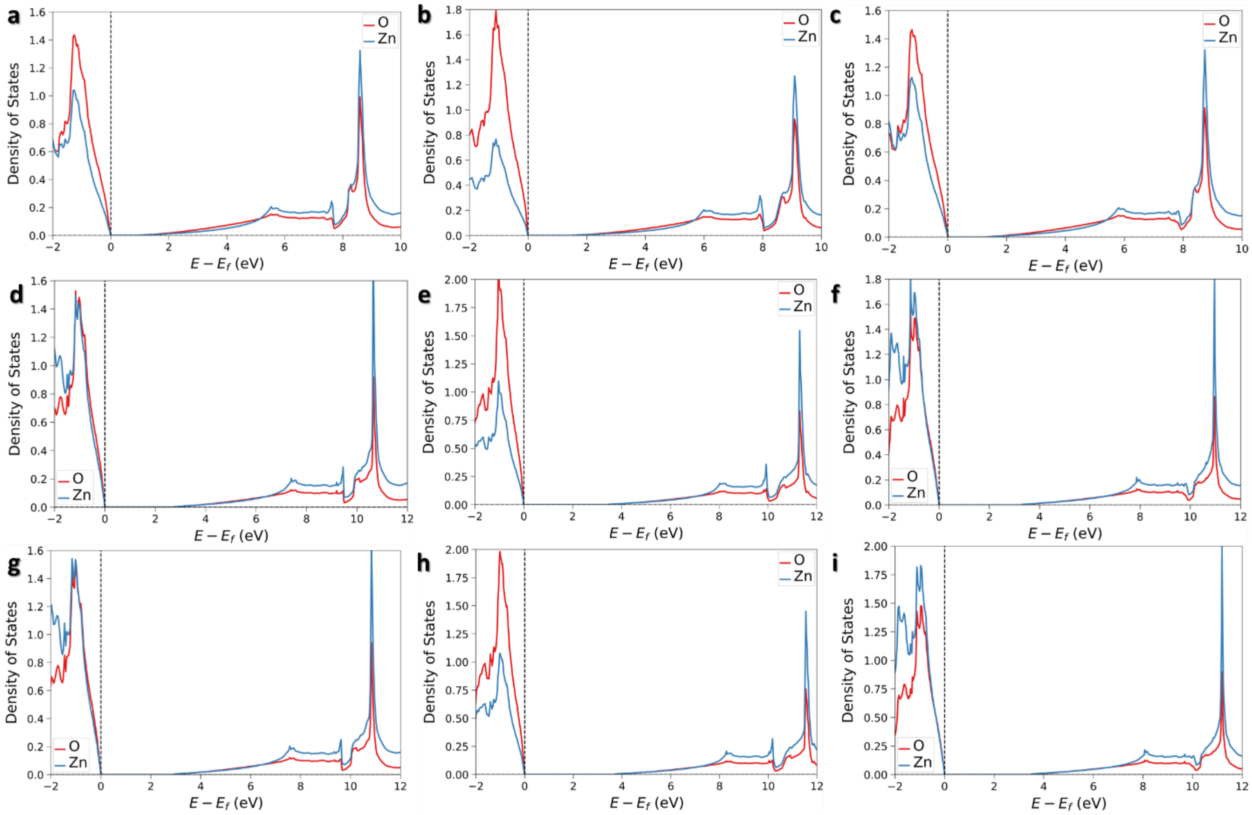

Figure S15: PDOS plots of the Zn 3*d* (red series) and O 2*p* (blue series) orbitals of pristine bulk ZnO zoomed-in to highlight band energies near E_F, systematically treated by functionals modelling correlation via PBE – with varied potential-only components – and different electronic structure models. PDOS for PBE functionals with **(a)** no Hubbard model, **(b)** $U_{Zn,3d}$ only, and **(c)** $U_{O,2p}$ only. PDOS for PBE-MBJ functionals with **(d)** no Hubbard model, **(e)** $U_{Zn,3d}$ only, and **(f)** $U_{O,2p}$ only. PDOS for PBE-LMBJ functionals with **(g)** no Hubbard model, **(h)** $U_{Zn,3d}$ only, and **(i)** $U_{O,2p}$ only.

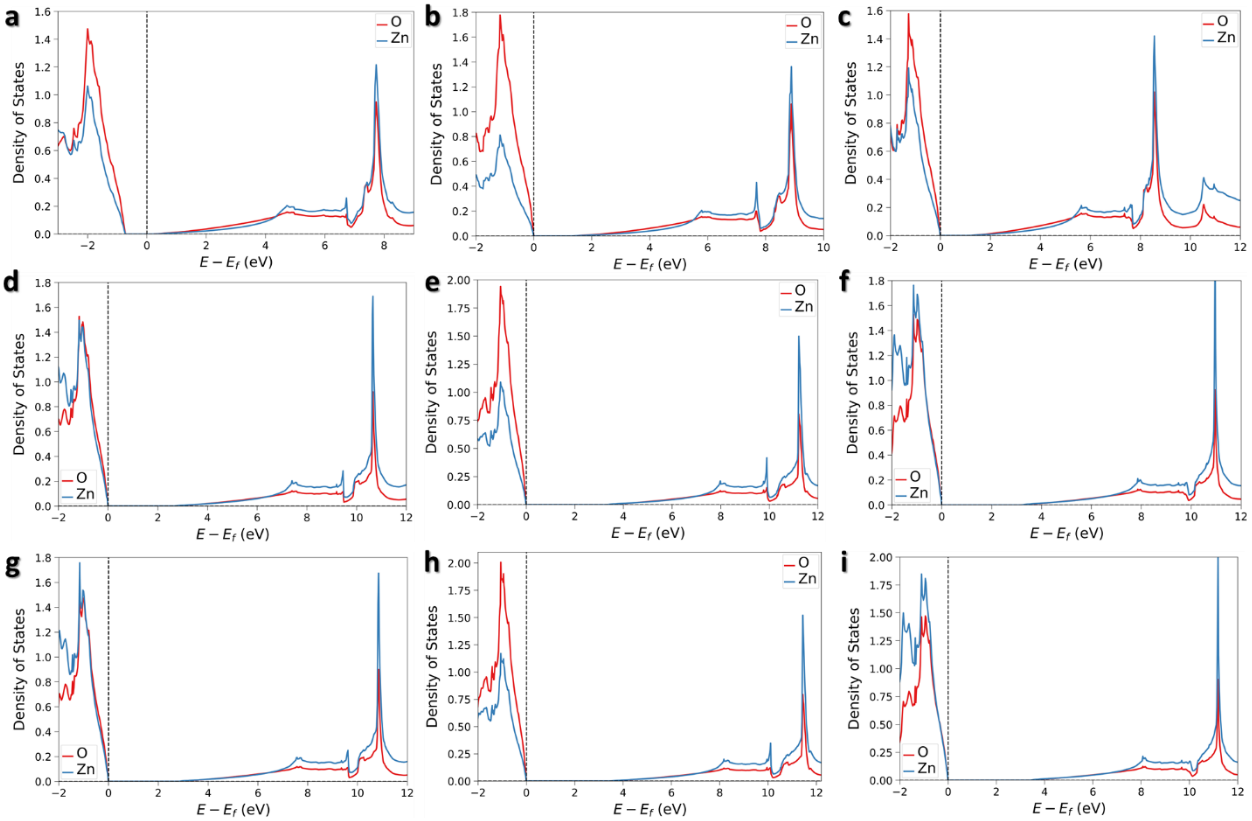

Figure S16: PDOS plots of the Zn 3*d* (blue series) and O 2*p* (red series) orbitals of pristine bulk ZnO zoomed-in to highlight band energies near E_F, systematically treated by functionals modelling correlation via PZ – with varied potential-only components – and different electronic structure models. **(a)** PDOS for PZ functionals with **(a)** no Hubbard model, **(b)** $U_{Zn,3d}$ only, and **(c)** $U_{O,2p}$ only. PDOS for PZ-MBJ functionals with **(d)** no Hubbard model, **(e)** $U_{Zn,3d}$ only, and **(f)** $U_{O,2p}$ only. PDOS for PZ-LMBJ functionals with **(g)** no Hubbard model, **(h)** $U_{Zn,3d}$ only, and **(i)** $U_{O,2p}$ only.

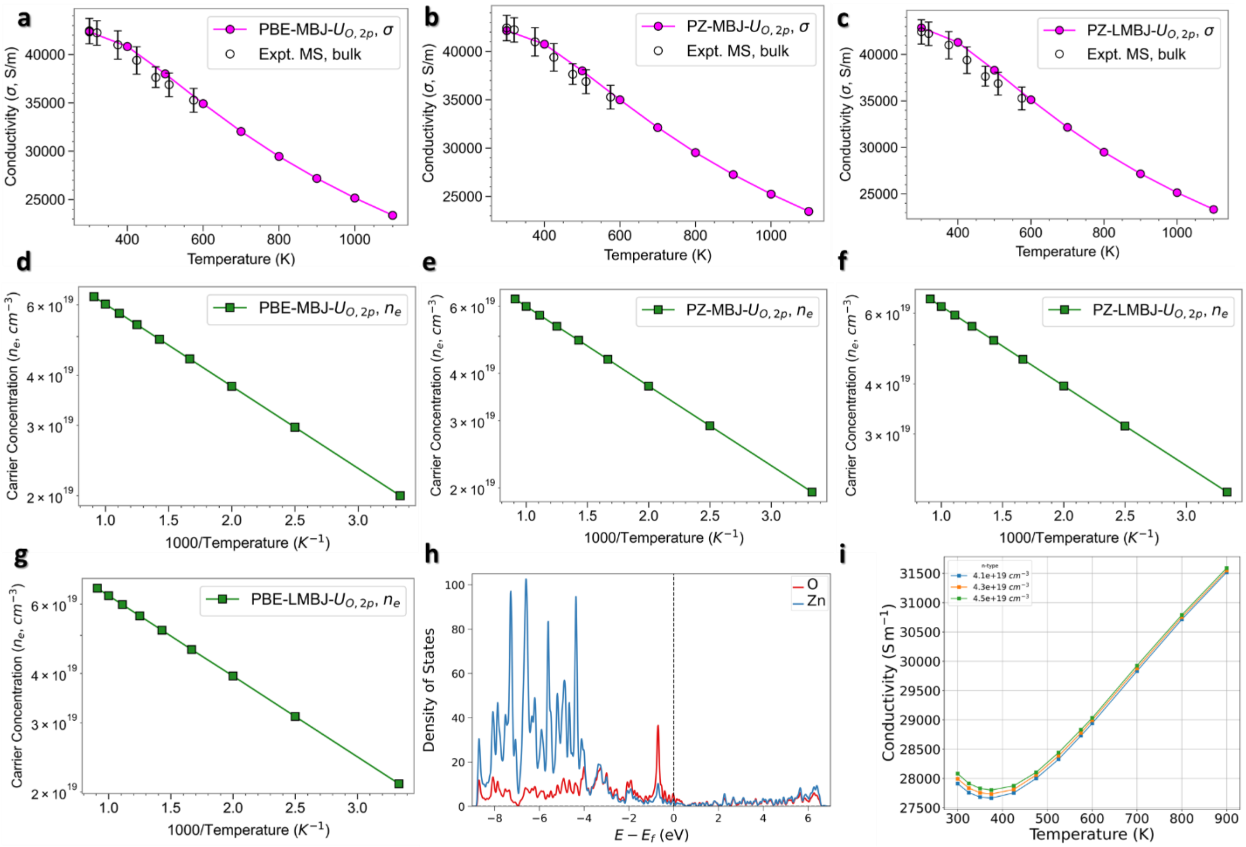

Figure S17: σ vs. *T* plots for bulk ZnO constructed using $U_{O,2p}$ electronic structure models, applying alternative functional pairs such as **(a)** PBE-MBJ, **(b)** PZ-MBJ, and **(c)** PZ-LMBJ. All simulated results were plotted with a corresponding experimental trend, featuring structures synthesized using Magnetron Sputtering (MS), consisting of resolved σ-T values and their uncertainties (error bars).[93] τ were empirically calculated from carrier concentrations (n_e) and *T*.[93,111] Simulated σ, which were closest to the endpoints of experimental trends, were scaled to match those experimental endpoints by ultimately varying only n_e, given temperature is fixed per σ and τ is calculated from n_e and temperature. Considering ln(n_e) vs. 1/T is a linear trend treatable as a quasi-chemical reaction, n_e was varied linearly to generate simulated σ-T profiles in bulk calculation. These linear relationships are plotted for **(d)** PBE-MBJ-$U_{O,2p}$, **(e)** PZ-MBJ-$U_{O,2p}$, **(f)** PZ-LMBJ-$U_{O,2p}$, and **(g)** PBE-LMBJ-$U_{O,2p}$ (σ-T plot in manuscript) models. Overall, all n_e ranges inputted into simulations subsume experimental values given over studied temperature domains (~2.0-6.4 x 10^{19} carriers/cm^{-3}).[93,110] **(h)** PDOS of simulated ZnO surface slabs taken from **Figure 3d**, parameterized via PBE-LMBJ-$U_{O,2p}$ models and depicting Zn 3*d* (blue series) and O 2*p* (red series) orbitals. Given E_g and related electronic structure features cannot be resolved from such plots both here and in previous literature,[120] the CRTA was applied to resolve τ, while n_e were selected via previous literature (4.3±0.2x10^{19} carriers/cm^3).[93] **(i)** Simulated σ-T profiles simulated for surface ZnO using PBE-LMBJ-$U_{O,2p}$ models, applying n_e = [4.1, 4.3, 4.5]x10^{19} carriers/cm^3 to visualize the impacts of uncertainty in n_e on σ-T.

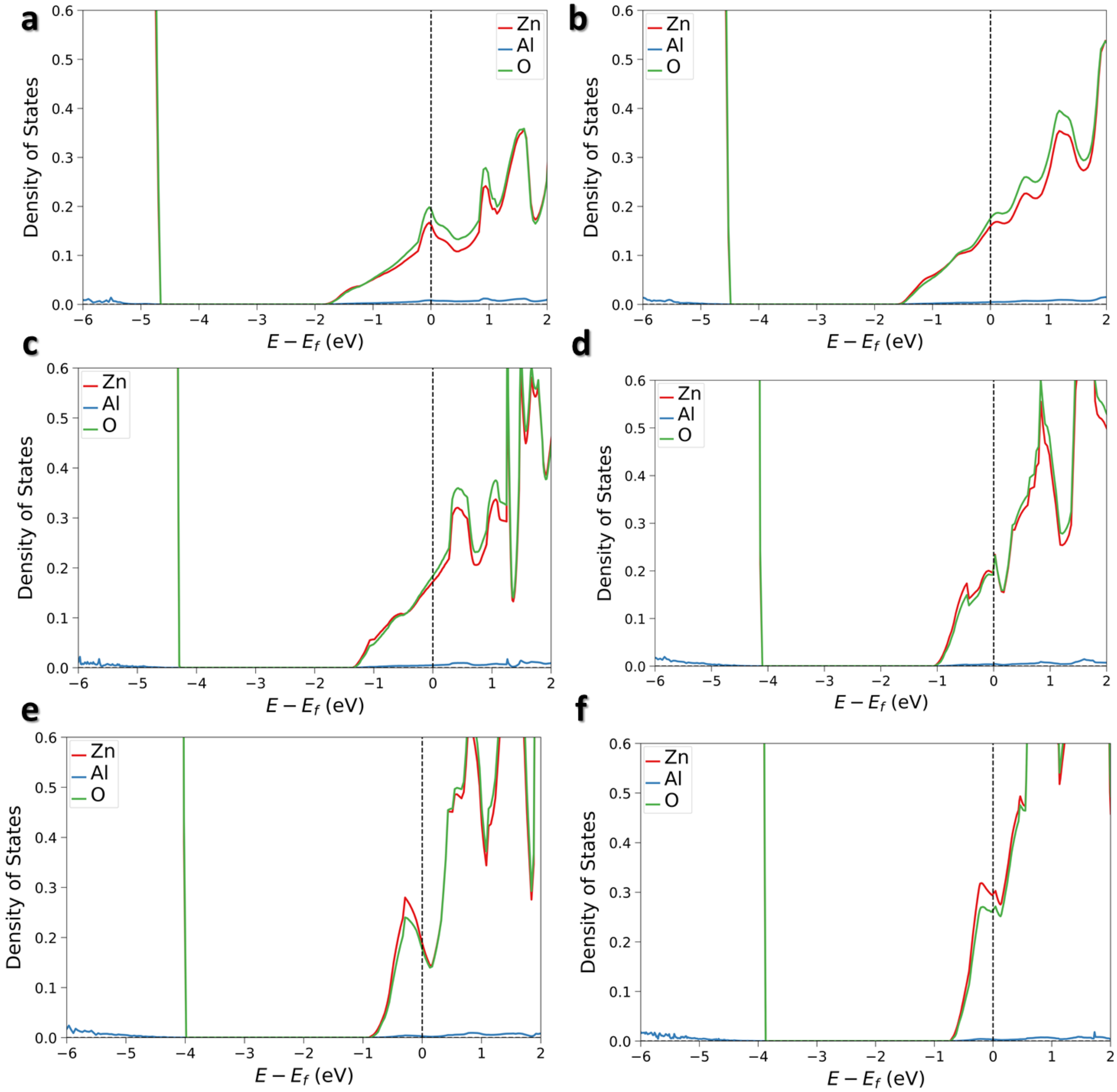

Figure S18: PDOS of AZO – with varied Al-dopant concentrations – consisting of O 2*p* (green series), Zn 3*d* (red series), and Al 3*p* (blue series) orbital character. PDOS are studied via LMBJ-PBE-$U_{O,2p}$ models adapted from ZnO, zooming in to depict Zn 3*d* and O 2*p* orbital states near E_F (dotted black lines). Here, AZO with Al-dopant concentrations of **(a)** 12.5 at.% Al ($Al_1Zn_7O_8$), **(b)** 8.33 at.% Al ($Al_1Zn_{11}O_{12}$), **(c)** 6.25 at.% Al ($Al_1Zn_{15}O_{16}$), **(d)** 4.16 at.% Al ($Al_1Zn_{23}O_{24}$), **(e)** 3.13 at.% Al ($Al_1Zn_{31}O_{32}$), and **(f)** 2.08 at.% Al ($Al_1Zn_{47}O_{48}$) are portrayed.

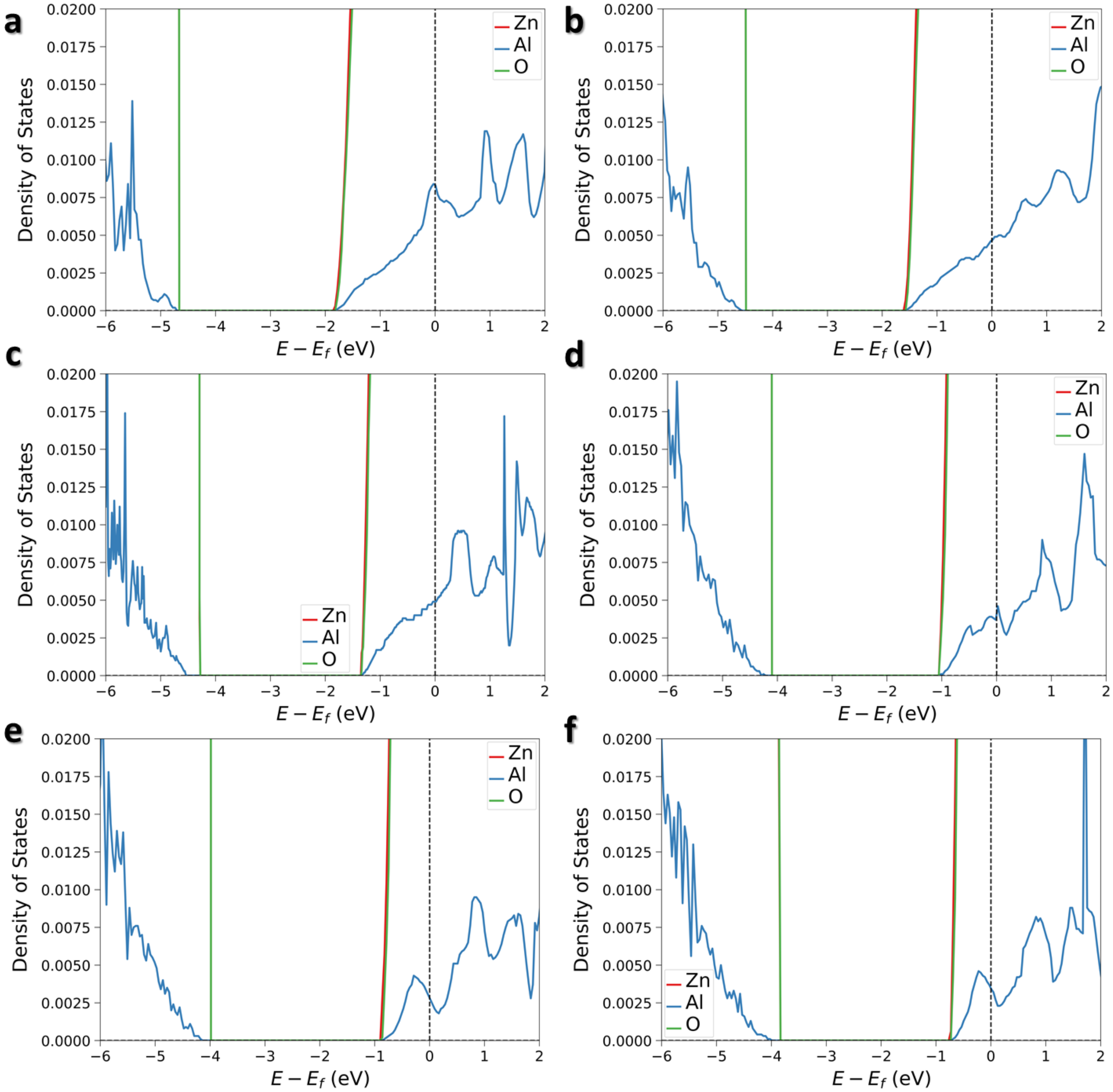

Figure S19: PDOS of AZO – with varied Al-dopant concentrations – consisting of O 2*p* (green series), Zn 3*d* (red series), and Al 3*p* (blue series) orbital character. PDOS are studied via LMBJ-PBE-$U_{\mathrm{O,2p}}$ models adapted from ZnO, zooming in to depict Al 3*p* orbital states near E_F (dotted black lines). Here, AZO with Al-dopant concentrations of **(a)** 12.5 at.% Al ($Al_1Zn_7O_8$), **(b)** 8.33 at.% Al ($Al_1Zn_{11}O_{12}$), **(c)** 6.25 at.% Al ($Al_1Zn_{15}O_{16}$), **(d)** 4.16 at.% Al ($Al_1Zn_{23}O_{24}$), **(e)** 3.13 at.% Al ($Al_1Zn_{31}O_{32}$), and **(f)** 2.08 at.% Al ($Al_1Zn_{47}O_{48}$) are portrayed.

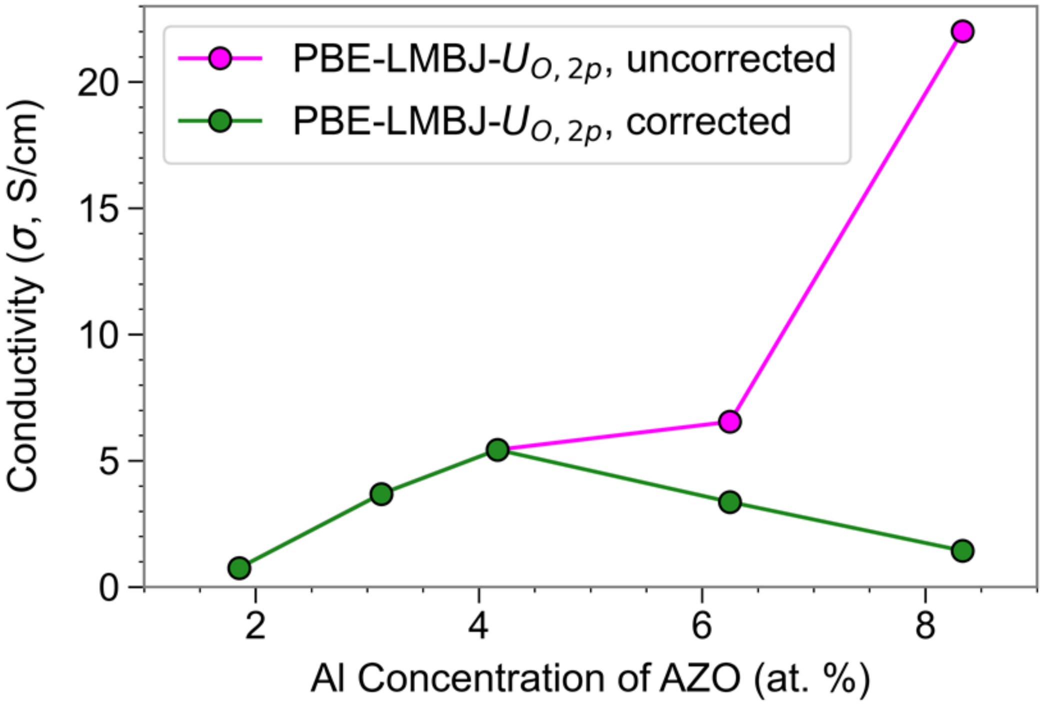

Figure S20: Comparison of PBE-LMBJ-$U_{O,2p}$ simulated σ vs. Al at.% trends correcting and not correcting for the quasi-kinetic regime switch between dominant electron-phonon and impurity contributions to τ. Uncorrected results, which were calculated using the PBE-LMBJ-$U_{O,2p}$ model and apply $\tau_{M\text{-}B}$ as a constant according to the CRTA, illustrate the effect of quasi-kinetic regime switch. This corresponds to discrepancies between corresponding experimental and simulated results in prior literature.[112]

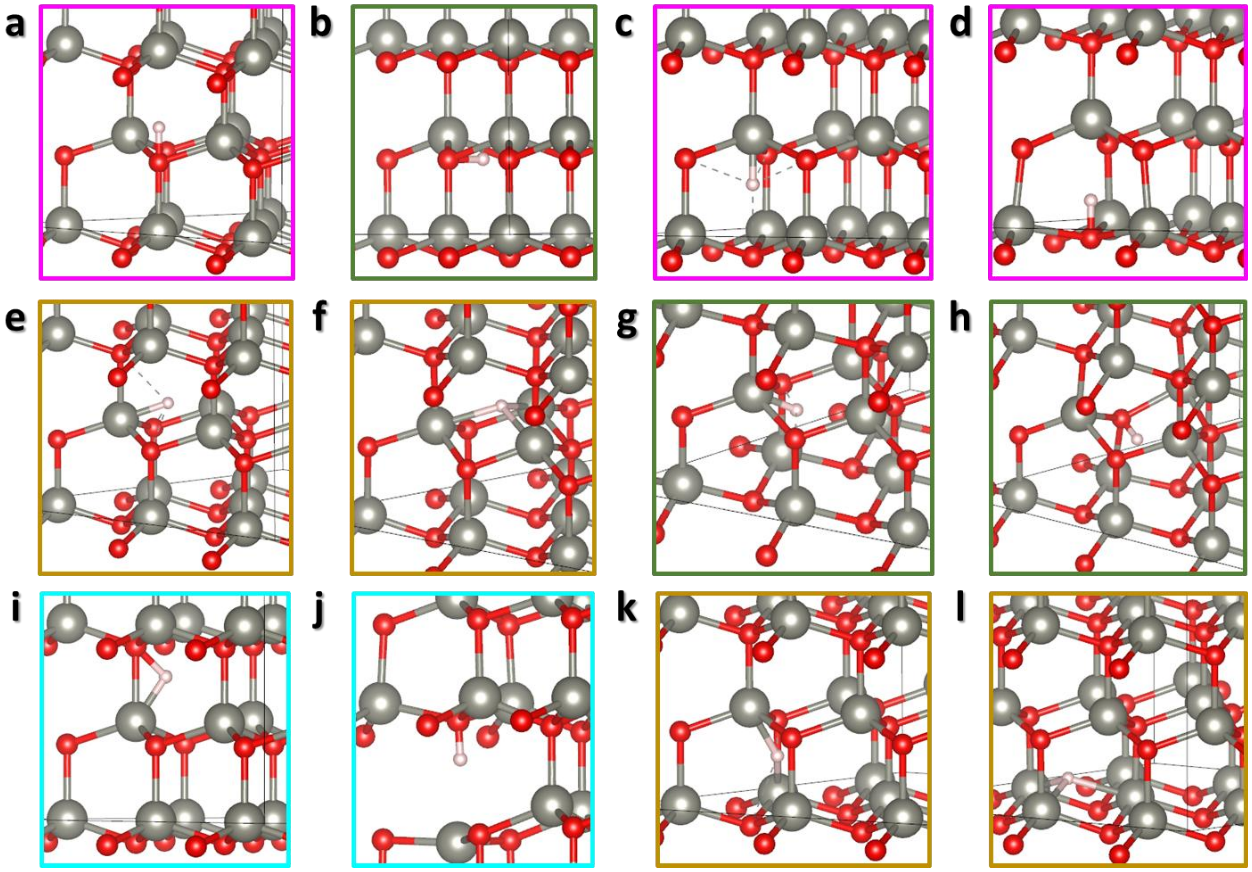

Figure S21: Systematically generated candidate H incorporation structures featuring 1 H and no defects in bulk ZnO ($1H_i$). Tested configurations adsorb single H to O in **(a)** axial (Ax.) and **(b)** equatorial (Eq.) positions, while single H that are **(c)** initially attached to Zn axially **(d)** relax to adjacent O axially and distort surrounding Zn-O tetrahedral shells (Sh.). Conversely, single H **(e)** initialized to Zn equatorially **(f)** relax to attach to 3 adjacent Zn atoms, while Zn **(g)** initially adsorbed to Zn and bound between two O **(h)** relax to O equatorially with distortion. H **(i)** initially bonded between O and Zn **(j)** relax to axially adsorb to O while breaking surrounding Zn-O tetrahedral shells (No Sh.), while corresponding H bonding **(k)** initialized between two Zn **(l)** relax to bond to 3 adjacent Zn. Over this configuration set, the most favorable structure yielded was (j), as depicted in Figure S25a (H-O Ax., No Sh.). Colored outlines around labelled atomic models correspond to the colors of graphed bars on plotted $E_{f,int}$ energies in Figure S25a when considering relaxed configurations, namely magenta (H-O Ax., Sh.: a, c, d), cyan (H-O Ax., No Sh.: i, j), green (H-O Eq.: b, g, h), and gold (H-Zn: e, f, k, l). Atomic models depicting H insertion feature Zn (dark grey), O (red), and H (white) atoms.

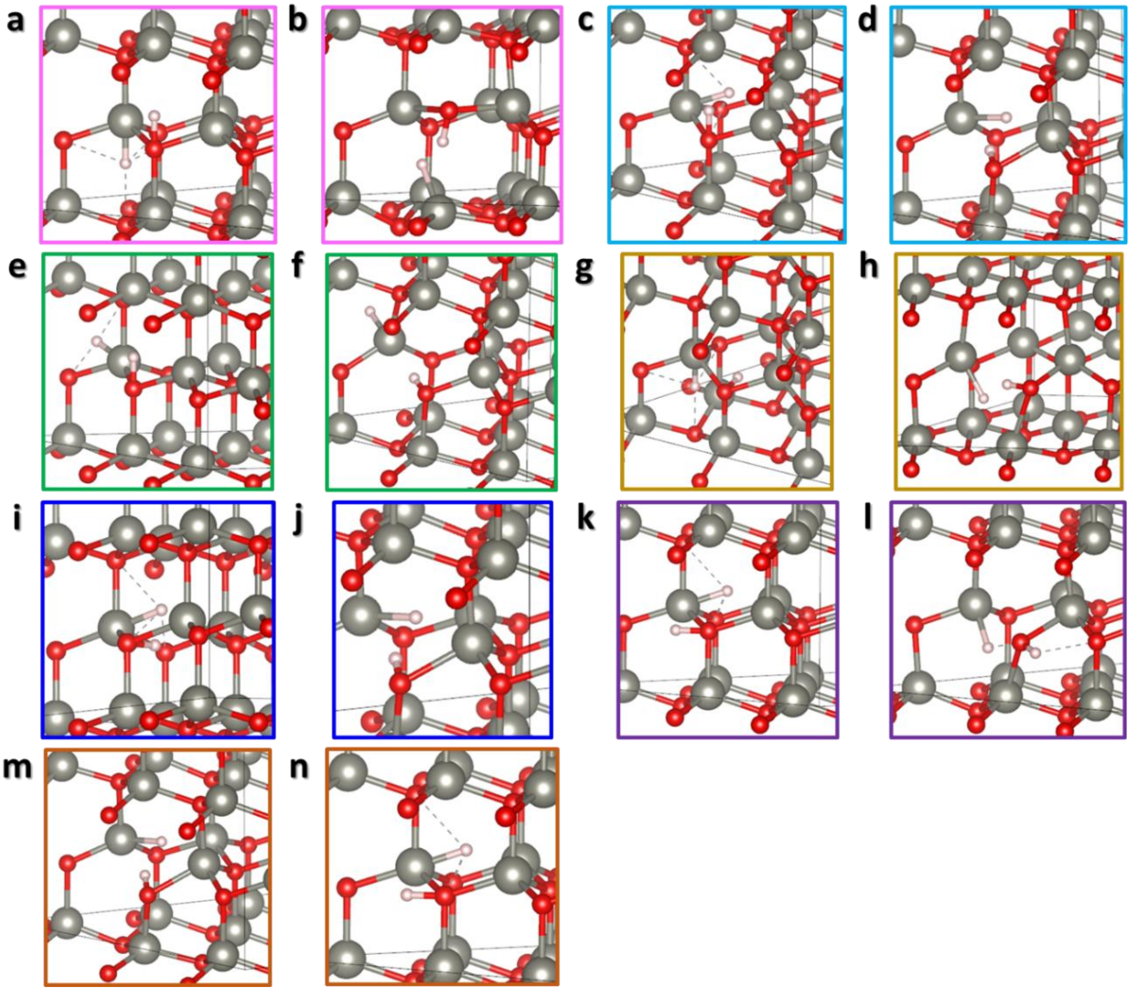

Figure S22: Systematically generated candidate H incorporation structures featuring 2 H and no defects in bulk ZnO ($2H_i$). Configurations **(a)** initially adsorb H to 1 axial O and 1 adjacent axial Zn (Ax.), though the **(b)** final structure relaxes H in a similar axial position directly underneath the other H. **(c)** Initializing 1 axial H on O and 1 equatorial (Eq.) H on Zn, **(d)** the final structure relaxes the H adsorbed to O into an equatorial position. **(e)** Initializing 1 axial H on O and 1 equatorial H on Zn in an inverted (Inv.) direction, **(f)** the final structure relaxes the H adsorbed to O into an equatorial position. **(g)** Initializing 1 equatorial H on O and 1 axial H on Zn **(h)** partially distorts the structure, as does **(i)** initializing 1 equatorial H on both O and Zn to **(j)** relax that structure. In contrast, **(k)** initializing 1 H each on O and Zn equatorially in inverted directions **(l)** relaxes H-Zn into an axial configuration. Also, **(m)** initializing 1 H each on O and Zn equatorially while only inverting 1 of these H **(n)** partially distorts the structure. Over this configuration set, the most favorable structure yielded was (j), as depicted in Figure S25b (H-O Eq., H-Zn Eq.). Colored outlines around labelled atomic models correspond to the colors of graphed bars on plotted $E_{f,int}$ energies in Figure S25b, which are defined according to either their initial (a-h) or final (i-l) configurations. Colors and bar graph labels include magenta (H-O Ax., H-Zn Ax.: a, b), cyan (H-O Ax., H-Zn Eq: c, d), green (H-O Ax., H-Zn Eq. Inv.: e, f), gold (H-O Eq., H-Zn Ax.: g, h), dark blue (H-O Eq., H-Zn Eq.: I, j), purple (H-O Eq. Inv., H-Zn Ax.: k, l), and orange (H-O Eq. Inv., H-Zn Eq.: k, l). Atomic models depicting H insertion feature Zn (dark grey), O (red), and H (white) atoms.

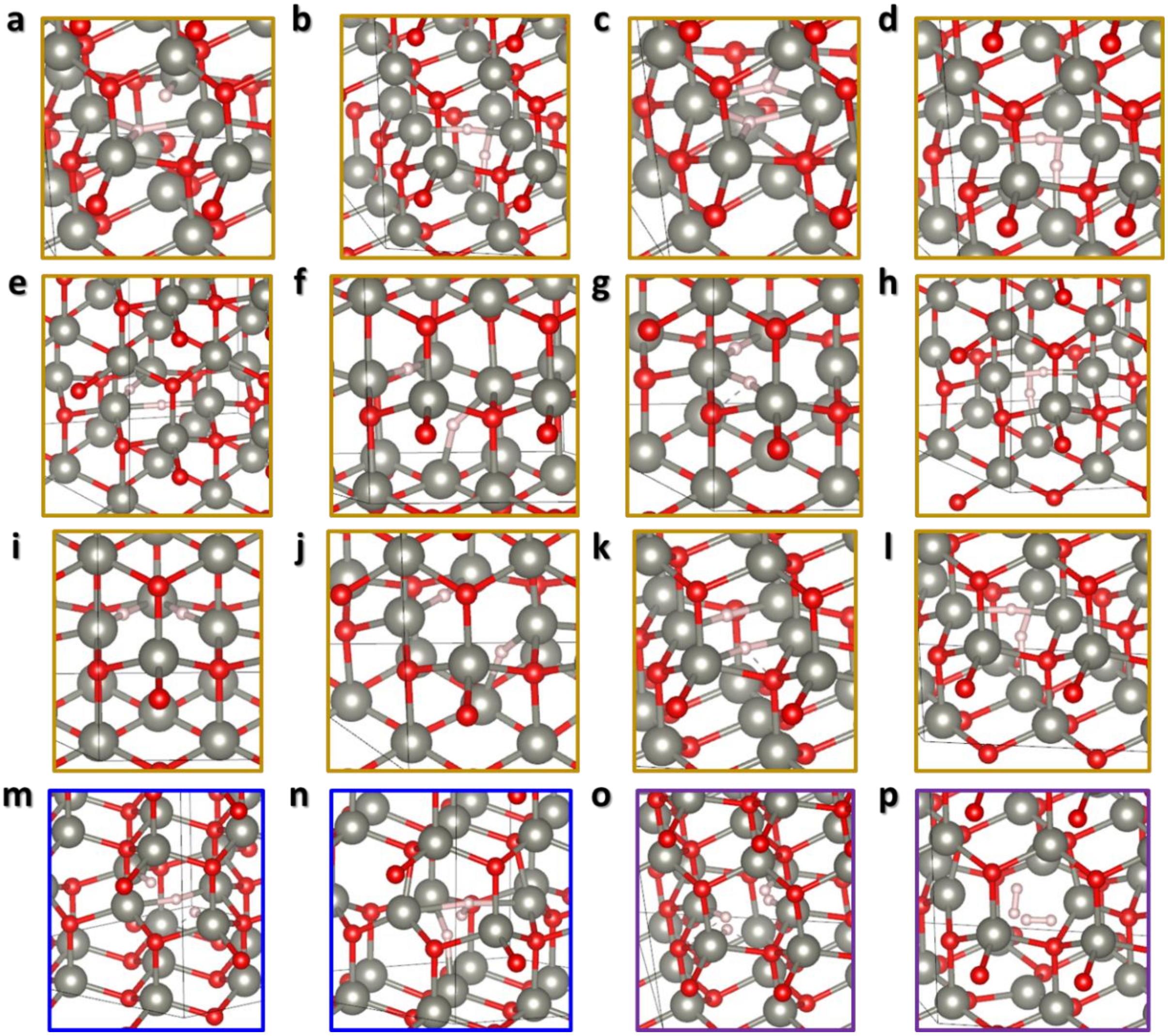

Figure S23: Systematically generated candidate H incorporation structures inserting more than 1 H into O vacancy defects in bulk ZnO (V_O-*n*H, *n*=1-4). Tested configurations adsorb 2 H **(a)** initially to separate Zn in 3-fold and 1-fold coordination to form a **(b)** relaxed structure, as well as **(c)** initially to separate Zn in solely 3-fold coordination that forms **(d)** the depicted relaxed structure. Also, 2 H adsorption is **(e)** initialized across Zn-H-Zn bonds that are 1 nearest neighbor (NN) away from each other to relax **(f)** accordingly. Corresponding 2 NN separated Zn-H-Zn bonds are concavely **(g)** initialized and **(h)** relaxed, as are corresponding 2 NN Zn-H-Zn bonds that are convexly **(i)** initialized and **(j)** relaxed. Similarly, Zn-H-Zn bonds that are arranged parallel to one other are **(k)** initialized and **(l)** relaxed. **(m)** Initialized and **(n)** relaxed configurations adsorbing 3 H into O vacancy defects. **(o)** Initialized and **(p)** relaxed configurations adsorbing 4 H into O vacancy defects. Colored outlines around labelled atomic models correspond to the colors of graphed bars on plotted $E_{f,int}$ energies in Figure S25c, which are defined according to their initial configurations. Only the most favorable $E_{f,int}$ are plotted per number of H inserted. Colors and bar graph labels include gold (a- l), dark blue (m-n), and purple (o-p). Atomic models depicting H insertion feature Zn (dark grey), O (red), and H (white) atoms.

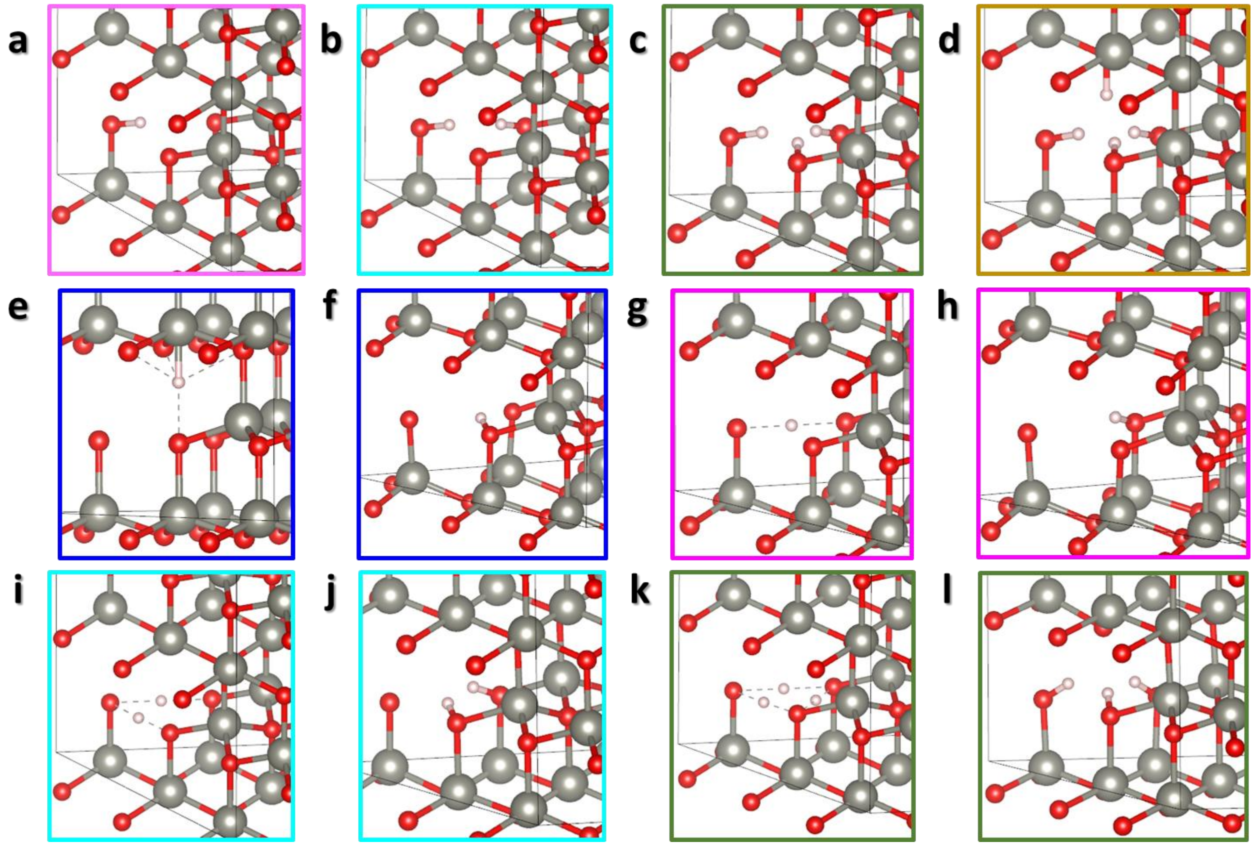

Figure S24: Systematically generated candidate H incorporation structures featuring various quantities of H adsorbed into Zn vacancy defects within bulk ZnO (V_{Zn}-nH, n=1-4). Tested configurations directly adsorb **(a)** 1, **(b)** 2, **(c)** 3, or **(d)** 4 H to individual undercoordinated O that tetrahedrally encompass Zn vacancy sites, while **(e)** initially H binding to undercoordinated Zn **(f)** relaxes to yield (a). **(g)** Initially adsorption of 1 H between two undercoordinated O **(h)** relaxes to reproduce (a), while **(i)** initializing 2 H between two similar pairs of O **(j)** reproduces (b) upon structural relaxation. **(k)** Initializing the corresponding operation with 3 H **(l)** induces relaxation to form (c). Over this configuration set, the most favorable structure yielded was (c), as depicted in Figure S24e (3H). Colored outlines around labelled atomic models correspond to the colors of graphed bars on plotted $E_{f,int}$ energies in Figure S25e, namely magenta (1H: a, g, h), cyan (2H: b, i, j), green (3H: c, k, l), gold (4H: d), and dark blue (H^-: e, f). Atomic models depicting H insertion feature Zn (dark grey), O (red), and H (white) atoms.

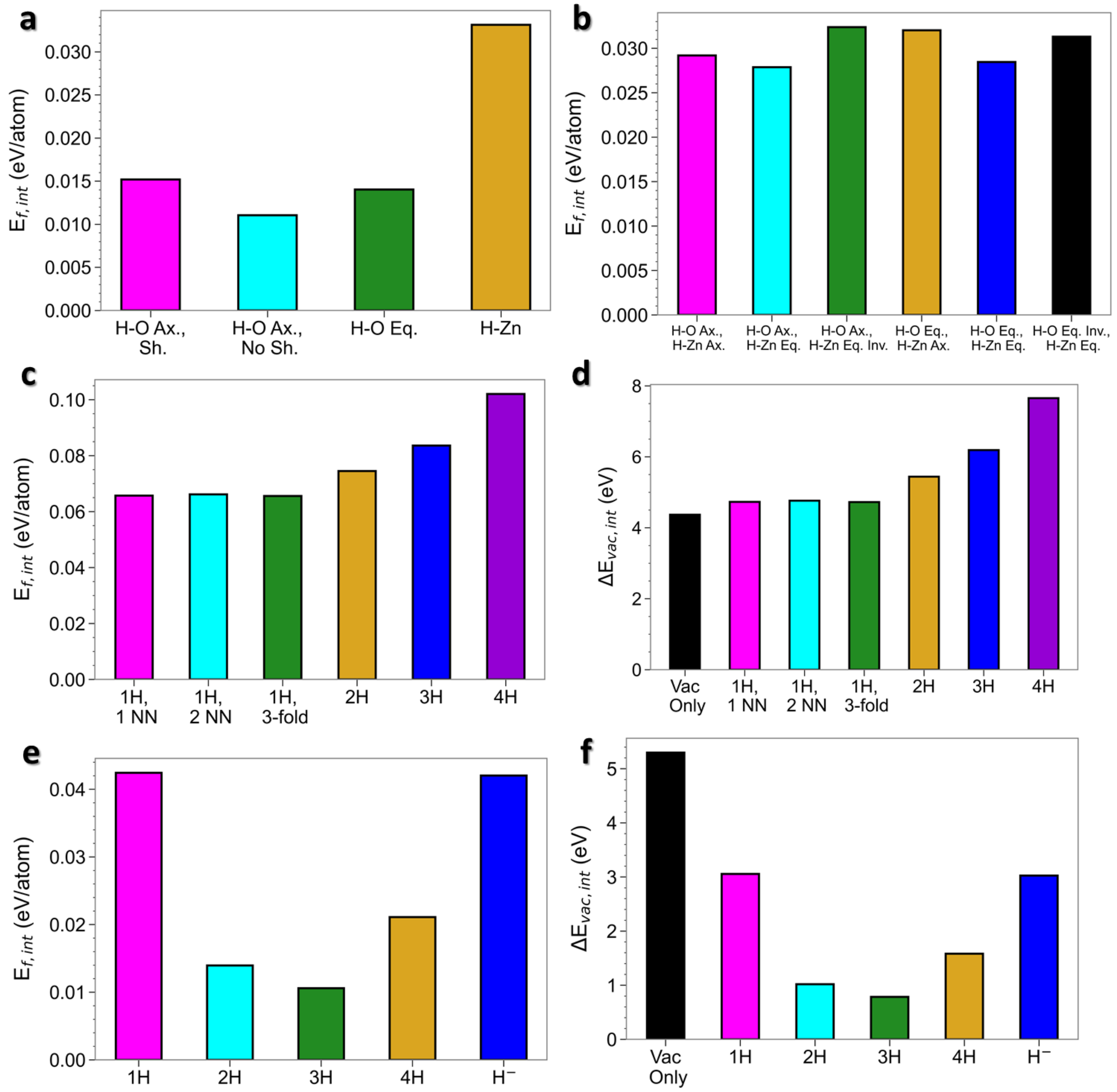

Figure S25: Energetics plots for ZnO atomic models depicted in **(a)** Figure S21 ($1H_i$), **(b)** Figure S22 ($2H_i$), **(c-d)** Figure S23 (V_O-nH for n=1-4), and **(e-f)** Figure S24 (V_{Zn}-nH for n=1-4). Though abbreviated labels in plots are more fully described in their respective plots containing atomic models, structures can be defined by the axial (Ax.) and equatorial (Eq.) configurations of their bonds, as well as the directional inversion (Inv.) of those bonds. Structures can also be labelled by the number of H they contain (for example: 1H and 2H), the coordination of those H relative to their nearest neighbors (for example: 1 NN and 3-fold), whether they only contain Zn or O vacancies ("Vac only"), and whether they contain H that were initially negatively charged by being bonded to Zn (H^-). Plotted quantities include $E_{f,int}$ in eV/atom (a-c, e) and $\Delta E_{vac,int}$ in eV (d, f). "1 H" systems in (c-d) are not visualized in Figure S23; "1 NN", "2 NN", and "3-fold" systems respectively describe single H initially adsorbed to 1, 2, or 3 nearest neighbor Zn atoms.

a

Composition	MPID
Al	mp-134
Zn	mp-79
O_2	mp-723285
H_2	mp-730101
Al_2ZnO_4	mp-2908
$Zn_{35}O_{36}H_4$	mp-2133 (ZnO)
Al_2O_3	mp-1143

b

Composition	MPID
Al	mp-134
Zn	mp-79
N_2	mp-154
O_2	mp-723285
Al_2ZnO_4	mp-2908
$Zn_{35}O_{36}H_3$	mp-2133 (ZnO)
Al_2O_3	mp-1143

c

Composition	MPID
Al	mp-134
Zn	mp-79
O_2	mp-723285
H_2	mp-730101
Al_2ZnO_4	mp-2908
$Zn_{35}O_{36}H_2$	mp-2133 (ZnO)
Al_2O_3	mp-1143
ZnO	mp-2133
$Al_1Zn_{95}O_{96}$	mp-2133 (ZnO)

d

Composition	MPID
Al	mp-134
Zn	mp-79
O_2	mp-723285
H_2	mp-730101
Al_2ZnO_4	mp-2908
Al_2O_3	mp-1143
ZnO	mp-2133
$Al_1Zn_{95}O_{96}$	mp-2133 (ZnO)

e

Composition	MPID
Al	mp-134
Zn	mp-79
O_2	mp-723285
H_2	mp-730101
Al_2ZnO_4	mp-2908
$Zn_{35}O_{36}H_2$	mp-2133 (ZnO)
$Zn_{35}O_{36}H_3$	mp-2133 (ZnO)
Al_2O_3	mp-1143
ZnO	mp-2133
$Al_1Zn_{95}O_{96}$	mp-2133 (ZnO)

f

Composition	MPID
AlN	mp-661
Zn	mp-79
O_2	mp-723285
H_2	mp-730101
Al_2ZnO_4	mp-2908
Al_2O_3	mp-1143
ZnN_2O_6	mp-772617
ZnO	mp-2133
$Al_1Zn_{95}O_{96}$	mp-2133 (ZnO)

g

Composition	MPID
AlN	mp-661
Zn	mp-79
O_2	mp-723285
H_2	mp-730101
Al_2ZnO_4	mp-2908
$Zn_{35}O_{36}H_2$	mp-2133 (ZnO)
Al_2O_3	mp-1143
ZnN_2O_6	mp-772617
ZnO	mp-2133
$Al_1Zn_{95}O_{96}$	mp-2133 (ZnO)

Table S26

Table S26: GCPD analyses of stable nitriding products developed by DFT under simulated SOFC conditions (600 °C, 0.5 atm) in the presence of steam, testing equilibration of coexisting N-based and H-based species to model H incorporation via hydride defect (V_{Zn}-nH, n=1-4) formation in bulk ZnO structures ($Zn_xO_xH_n$, x>2, n=1-4). When modeling NH_3 or N_2 nitriding in the presence of H, which is yielded from the decomposition of steam (H_2O) via ZnO surface interactions, the ratios of corresponding N-based and H-based chemical potentials (μ_{NH3}/μ_{H2}) are represented as respective equilibrated NH_3/N_2 and H_2 reactant (input) gas concentration ratios. Applying this framework referenced with respect to the magnitude of μ_{NH3}, GCPD analyses of NH_3 nitriding yielded distinct final stable phases when equilibrated reactant μ_{NH3}/μ_{H2} ratios were set to **(a)** 4:1, **(b)** 3:1, **(c)** 2:1, and **(d)** 5:3. Corresponding results for N_2 nitriding, completed using equal μ_{N2}/μ_{H2} ratios, achieved equivalent results. Decomposing 1 mol of NH_3 yields stoichiometric quantities of N_2 (0.5 mol) and H_2 (1.5 mol), while subsequent decomposition of H_2 on ZnO surfaces yields dissociated H adsorbates (0.5 H_2). To represent these nitriding reaction environments, corresponding GCPD analyses including hydride structures have evaluated stoichiometrically weighted chemical potential proportions, representing equilibrated reactant gas ratios, of **(e)** NH_3 only (μ_{H2}/μ_{NH3}=0), **(f)** 0.5 N_2 and 1.5 H_2 (μ_{N2}/μ_{H2}=1:3), and **(g)** 0.5 N_2 and 0.5 H_2 (μ_{N2}/μ_{H2}=1:1).

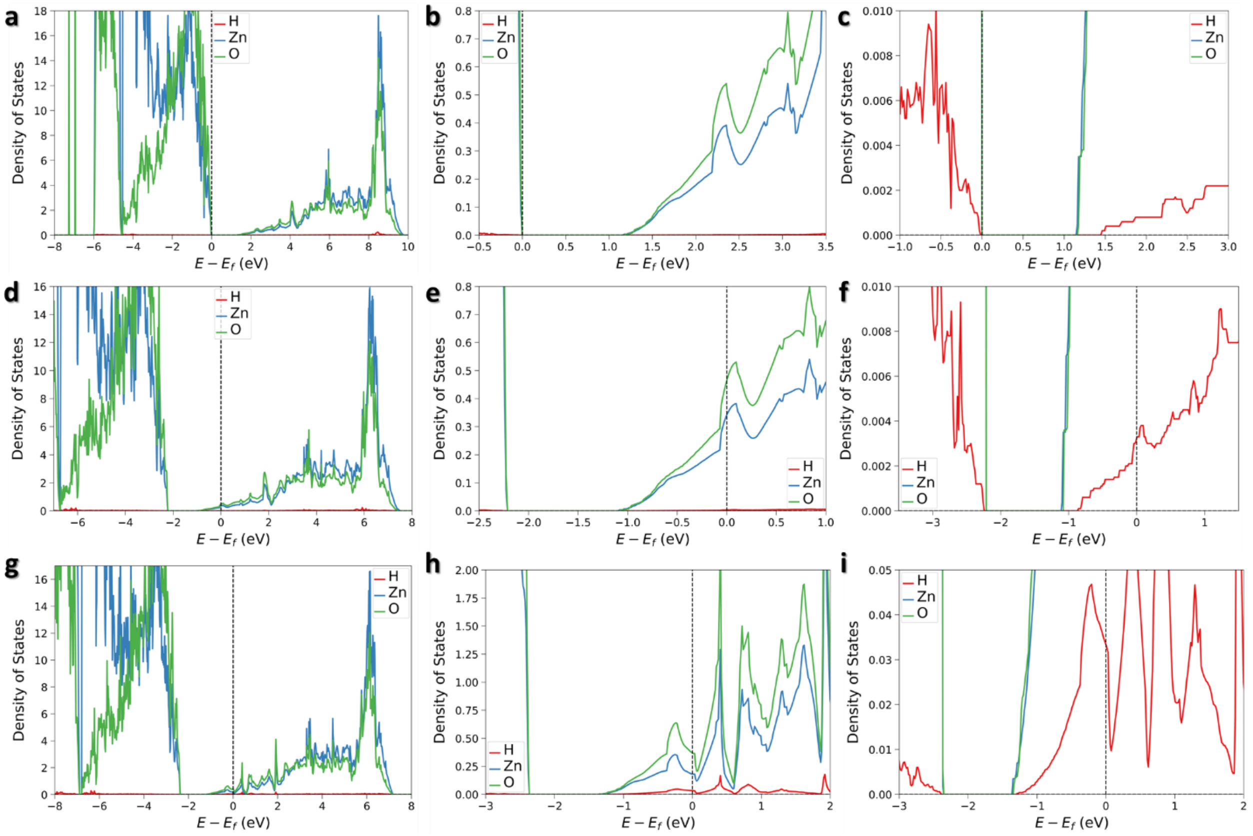

Figure S27: PDOS plots depicting electronic structures of V_{Zn}-nH (n=2-4) around E_F (dotted black lines), portraying H 1*s* (red series), Zn 3*d* (blue series), and O 2*p* (green series) orbitals. PDOS for V_{Zn}-2H emphasize **(a)** overall orbital character, **(b)** Zn 3*d* and O 2*p* contributions near E_F, and **(c)** H 1*s* contributions near E_F. PDOS for V_{Zn}-3H emphasize **(d)** overall orbital character, **(e)** Zn 3*d* and O 2*p* contributions near E_F, and **(f)** H 1*s* contributions near E_F. PDOS for V_{Zn}-4H emphasize **(g)** overall orbital character, **(h)** Zn 3*d* and O 2*p* contributions near E_F, and **(i)** H 1*s* contributions near E_F.

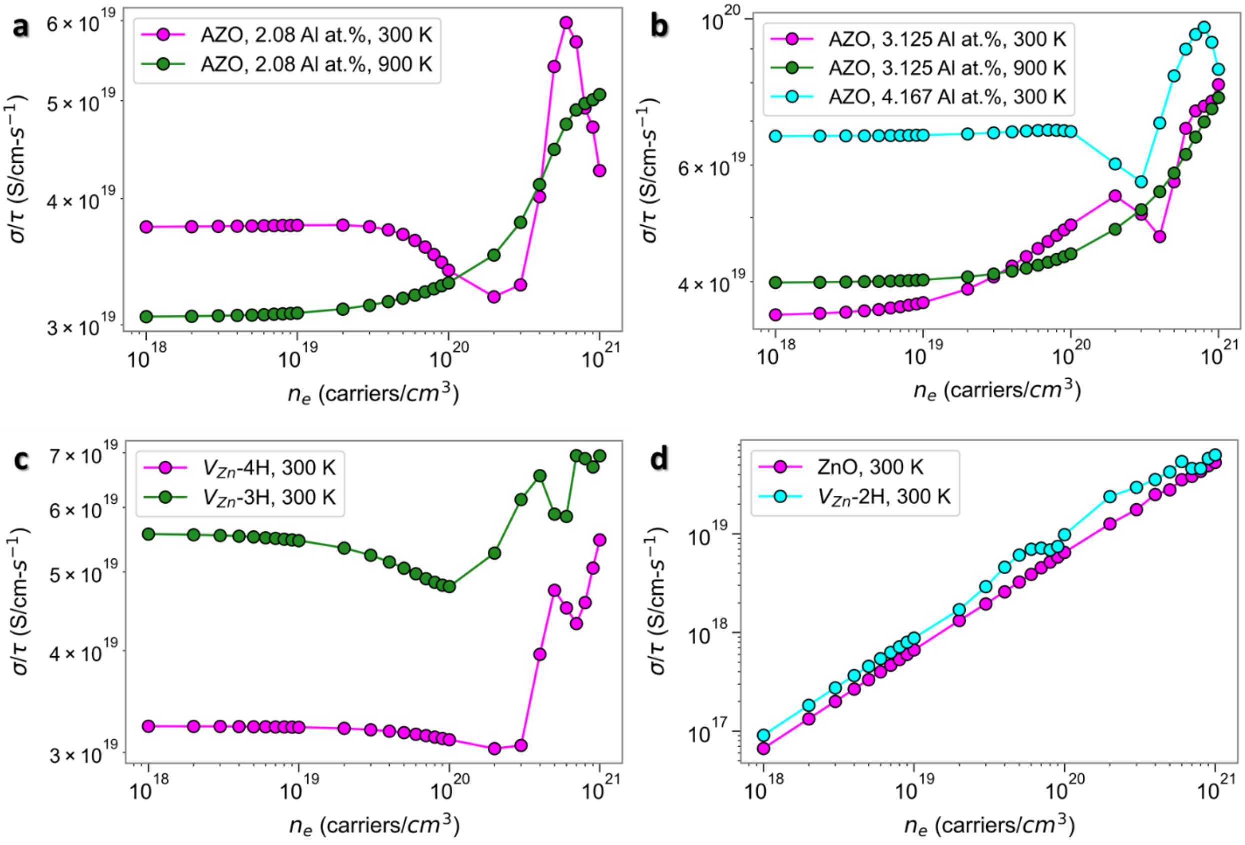

Figure S28: CRTA profiles (σ/τ vs. n_e) of **(a)** of bulk AZO at 2.08 Al at.% at 300 and 900 K, **(b)** bulk AZO with 3.125 Al at.% at 300 & 900 K and 4.167 Al at.% at 300 K, **(c)** V_{Zn}-4H & V_{Zn}-3H at 300 K, and **(d)** V_{Zn}-2H & ZnO at 300 K.

References

1 G. Kresse and J. Furthmüller, *Phys Rev B*, 1996, **54**, 11169–11186.

2 B. Deng, P. Zhong, K. Jun, J. Riebesell, K. Han, C. J. Bartel and G. Ceder, *Nat Mach Intell*, 2023, **5**, 1031–1041.

3 J. P. Perdew, K. Burke and M. Ernzerhof, *Phys Rev Lett*, 1996, **77**, 3865–3868.

4 M. Ernzerhof and G. E. Scuseria, *J Chem Phys*, 1999, **110**, 5029–5036.

5 G. Kresse and D. Joubert, *Phys Rev B*, 1999, **59**, 1758–1775.

6 M. T. Curnan and J. R. Kitchin, *The Journal of Physical Chemistry C*, 2014, **118**, 28776–28790.

7 M. T. Curnan and J. R. Kitchin, *The Journal of Physical Chemistry C*, 2015, **119**, 21060–21071.

8 A. Jain, S. P. Ong, G. Hautier, W. Chen, W. D. Richards, S. Dacek, S. Cholia, D. Gunter, D. Skinner, G. Ceder and K. A. Persson, *APL Mater*, 2013, **1**, 11002.

9 H. Chi, M. T. Curnan, M. Li, C. M. Andolina, W. A. Saidi, G. Veser and J. C. Yang, *Physical Chemistry Chemical Physics*, 2020, **22**, 2738–2742.

10 H. Chi, C. M. Andolina, J. Li, M. T. Curnan, W. A. Saidi, G. Zhou, J. C. Yang and G. Veser, *Appl Catal A Gen*, 2018, **556**, 64–72.

11 F. Maldonado and A. Stashans, *Journal of Physics and Chemistry of Solids*, 2010, **71**, 784–787.

12 J. E. Saal, S. Kirklin, M. Aykol, B. Meredig and C. Wolverton, *JOM*, 2013, **65**, 1501–1509.

13 S. Kirklin, J. E. Saal, B. Meredig, A. Thompson, J. W. Doak, M. Aykol, S. Rühl and C. Wolverton, *NPJ Comput Mater*, 2015, **1**, 15010.

14 R. Gholizadeh, Y.-X. Yu and Y. Wang, *Appl Surf Sci*, 2017, **420**, 944–953.

15 A. F. Carley, S. Yan and M. W. Roberts, *Journal of the Chemical Society, Faraday Transactions*, 1990, **86**, 2701–2710.

16 T. Hasegawa, Y. Shirotori, K. Ozawa, K. Edamoto and K. Takahashi, *Appl Surf Sci*, 2004, **237**, 352–357.

17 C. T. Au, M. W. Roberts and R. Mason, *Proceedings of the Royal Society of London. A. Mathematical and Physical Sciences*, 1997, **396**, 165–181.

18 R. Huang, Y. Zhu, M. T. Curnan, Y. Zhang, J. W. Han, Y. Chen, S. Huang and Z. Lin, *Cell Rep Phys Sci*, 2021, **2**, 1–17.

19 M. T. Curnan, C. M. Andolina, M. Li, Q. Zhu, H. Chi, W. A. Saidi and J. C. Yang, *The Journal of Physical Chemistry C*, 2019, **123**, 452–463.

20 M. Li, M. T. Curnan, M. A. Gresh-Sill, S. D. House, W. A. Saidi and J. C. Yang, *Nat Commun*, 2021, **12**, 2781.

21 X. Duan, J. Ji, G. Qian, C. Fan, Y. Zhu, X. Zhou, D. Chen and W. Yuan, *J Mol Catal A Chem*, 2012, **357**, 81–86.

22 J. Villafuerte, F. Donatini, J. Kioseoglou, E. Sarigiannidou, O. Chaix-Pluchery, J. Pernot and V. Consonni, *The Journal of Physical Chemistry C*, 2020, **124**, 16652–16662.

23 J. Villafuerte, E. Sarigiannidou, F. Donatini, J. Kioseoglou, O. Chaix-Pluchery, J. Pernot and V. Consonni, *Nanoscale Adv*, 2022, **4**, 1793–1807.

24 S. P. Ong, S. Cholia, A. Jain, M. Brafman, D. Gunter, G. Ceder and K. A. Persson, *Comput Mater Sci*, 2015, **97**, 209–215.

25 C. J. Bartel, *J Mater Sci*, 2022, **57**, 10475–10498.

26 J. Guo, L. Guan, S. Wang, Q. Zhao, Y. Wang and B. Liu, *Appl Surf Sci*, 2008, **255**, 3164–3169.

27 Z. Mansouri, A. Sibari, A. Al-Shami, S. Lahbabi, A. El Kenz, A. Benyoussef, A. El Fatimy and O. Mounkachi, *Comput Mater Sci*, DOI:10.1016/j.commatsci.2021.110936.

28 P. Virtanen, R. Gommers, T. E. Oliphant, M. Haberland, T. Reddy, D. Cournapeau, E. Burovski, P. Peterson, W. Weckesser, J. Bright, S. J. van der Walt, M. Brett, J. Wilson, K. J. Millman, N. Mayorov, A. R. J. Nelson, E. Jones, R. Kern, E. Larson, C. J. Carey, İ. Polat, Y. Feng, E. W. Moore, J. VanderPlas, D. Laxalde, J. Perktold, R. Cimrman, I. Henriksen, E. A. Quintero, C. R. Harris, A. M. Archibald, A. H. Ribeiro, F. Pedregosa, P. van Mulbregt, A. Vijaykumar, A. Pietro Bardelli, A. Rothberg, A. Hilboll, A. Kloeckner, A. Scopatz, A. Lee, A. Rokem, C. N. Woods, C. Fulton, C. Masson, C. Häggström, C. Fitzgerald, D. A. Nicholson, D. R. Hagen, D. V Pasechnik, E. Olivetti, E. Martin, E. Wieser, F. Silva, F. Lenders, F. Wilhelm, G. Young, G. A. Price, G.-L. Ingold, G. E. Allen, G. R. Lee, H. Audren, I. Probst, J. P. Dietrich, J. Silterra, J. T. Webber, J. Slavič, J. Nothman, J. Buchner, J. Kulick, J. L. Schönberger, J. V. de Miranda Cardoso, J. Reimer, J. Harrington, J. L. C. Rodríguez, J. Nunez-Iglesias, J. Kuczynski, K. Tritz, M. Thoma, M. Newville, M. Kümmerer, M. Bolingbroke, M. Tartre, M. Pak, N. J. Smith, N. Nowaczyk, N. Shebanov, O. Pavlyk, P. A. Brodtkorb, P. Lee, R. T. McGibbon, R. Feldbauer, S. Lewis, S. Tygier, S. Sievert, S. Vigna, S. Peterson, S. More, T. Pudlik, T. Oshima, T. J. Pingel, T. P. Robitaille, T. Spura, T. R. Jones, T. Cera, T. Leslie, T. Zito, T. Krauss, U. Upadhyay, Y. O. Halchenko, Y. Vázquez-Baeza and S. 1. 0 Contributors, *Nat Methods*, 2020, **17**, 261–272.

29 A. Wang, R. Kingsbury, M. McDermott, M. Horton, A. Jain, S. P. Ong, S. Dwaraknath and K. A. Persson, *Sci Rep*, 2021, **11**, 15496.

30 A. Jain, G. Hautier, S. P. Ong, C. J. Moore, C. C. Fischer, K. A. Persson and G. Ceder, *Phys Rev B*, 2011, **84**, 045115.

31 M. Aykol, S. S. Dwaraknath, W. Sun and K. A. Persson, *Sci Adv*, 2018, **4**, eaaq0148.

32 S. P. Ong, L. Wang, B. Kang and G. Ceder, *Chemistry of Materials*, 2008, **20**, 1798–1807.

33 S. P. Ong, A. Jain, G. Hautier, B. Kang and G. Ceder, *Electrochem commun*, 2010, **12**, 427–430.

34 S. H. Achour, *Zenodo*, 2023, preprint, DOI: 10.5281/zenodo.7761303.

35 A. Hjorth Larsen, J. Jørgen Mortensen, J. Blomqvist, I. E. Castelli, R. Christensen, M. Dułak, J. Friis, M. N. Groves, B. Hammer, C. Hargus, E. D. Hermes, P. C. Jennings, P. Bjerre Jensen, J. Kermode, J. R. Kitchin, E. Leonhard Kolsbjerg, J. Kubal, K. Kaasbjerg, S. Lysgaard, J. Bergmann Maronsson, T. Maxson, T. Olsen, L. Pastewka, A. Peterson, C. Rostgaard, J. Schiøtz, O. Schütt, M. Strange, K. S. Thygesen, T. Vegge, L. Vilhelmsen, M. Walter, Z. Zeng and K. W. Jacobsen, *Journal of Physics: Condensed Matter*, 2017, **29**, 273002.

36 D. A. McQuarrie, *Statistical Mechanics*, University Science Books, 1st edn., 2000.

37 C. J. Cramer, *Essentials of computational chemistry: theories and models*, John Wiley & Sons, 2nd edn., 2004.

38 L. Wang, T. Maxisch and G. Ceder, *Phys Rev B*, 2006, **73**, 195107.

39 D. Bora, F. R. Gayen and B. Saha, *RSC Adv*, 2022, **12**, 33567–33583.

40 M. H. Stans, *NIST Spec. Publ*, 1970, **1**, 1–48.

41 R. Urrego-Ortiz, S. Builes, F. Illas and F. Calle-Vallejo, *EES Catalysis*, 2024, **2**, 157–179.

42 J. P. Perdew, J. A. Chevary, S. H. Vosko, K. A. Jackson, M. R. Pederson, D. J. Singh and C. Fiolhais, *Phys Rev B*, 1992, **46**, 6671–6687.

43 Y. Zhang and W. Yang, *Phys Rev Lett*, 1998, **80**, 890.

44 B. Hammer, L. B. Hansen and J. K. Nørskov, *Phys Rev B*, 1999, **59**, 7413–7421.

45 J. P. Perdew, A. Ruzsinszky, G. I. Csonka, O. A. Vydrov, G. E. Scuseria, L. A. Constantin, X. Zhou and K. Burke, *Phys Rev Lett*, 2008, **100**, 136406.

46 A. E. Mattsson and R. Armiento, *Phys Rev B*, 2009, **79**, 155101.

47 R. Armiento and A. E. Mattsson, *Phys Rev B*, 2005, **72**, 85108.

48 A. E. Mattsson, R. Armiento, J. Paier, G. Kresse, J. M. Wills and T. R. Mattsson, *J Chem Phys*, 2008, **128**, 084714.

49 J. Wellendorff, K. T. Lundgaard, A. Møgelhøj, V. Petzold, D. D. Landis, J. K. Nørskov, T. Bligaard and K. W. Jacobsen, *Phys Rev B*, 2012, **85**, 235149.

50 J. Sun, A. Ruzsinszky and J. P. Perdew, *Phys Rev Lett*, 2015, **115**, 36402.

51 A. P. Bartók and J. R. Yates, *J Chem Phys*, 2019, **150**, 161101.

52 J. W. Furness, A. D. Kaplan, J. Ning, J. P. Perdew and J. Sun, *J Phys Chem Lett*, 2020, **11**, 8208–8215.

53 D. Mejia-Rodriguez and S. B. Trickey, *Phys Rev B*, 2018, **98**, 115161.

54 D. Mejia-Rodriguez and S. B. Trickey, *Phys Rev A (Coll Park)*, 2017, **96**, 52512.

55 M. Všianská and M. Šob, *Solid State Sci*, 2024, **157**, 107709.

56 A. D. Kaplan and J. P. Perdew, *Phys Rev Mater*, 2022, **6**, 83803.

57 D. Mejía-Rodríguez and S. B. Trickey, *Phys Rev B*, 2020, **102**, 121109.

58 J. Tao, J. P. Perdew, V. N. Staroverov and G. E. Scuseria, *Phys Rev Lett*, 2003, **91**, 146401.

59 J. P. Perdew, A. Ruzsinszky, G. I. Csonka, L. A. Constantin and J. Sun, *Phys Rev Lett*, 2009, **103**, 26403.

60 J. Sun, R. Haunschild, B. Xiao, I. W. Bulik, G. E. Scuseria and J. P. Perdew, *J Chem Phys*, 2013, **138**, 044113.

61 J. Sun, B. Xiao and A. Ruzsinszky, *J Chem Phys*, 2012, **137**, 051101.

62 H. Francisco, A. C. Cancio and S. B. Trickey, *J Chem Phys*, 2023, **159**, 214102.

63 J. Tao and Y. Mo, *Phys Rev Lett*, 2016, **117**, 73001.

64 H. Francisco, A. C. Cancio and S. B. Trickey, *J Chem Phys*, 2023, **159**, 214103.

65 A. D. Becke and E. R. Johnson, *J Chem Phys*, 2006, **124**, 221101.

66 F. Tran and P. Blaha, *Phys Rev Lett*, 2009, **102**, 226401.

67 T. Rauch, M. A. L. Marques and S. Botti, *Phys Rev B*, 2020, **101**, 245163.

68 T. Rauch, M. A. L. Marques and S. Botti, *J Chem Theory Comput*, 2020, **16**, 2654–2660.

69 J. P. Perdew, M. Ernzerhof and K. Burke, *J Chem Phys*, 1996, **105**, 9982–9985.

70 C. Adamo and V. Barone, *J Chem Phys*, 1999, **110**, 6158–6170.

71 J. C. Slater, *Physical Review*, 1951, **81**, 385–390.

72 A. V Krukau, O. A. Vydrov, A. F. Izmaylov and G. E. Scuseria, *J Chem Phys*, 2006, **125**, 224106.

73 J. Heyd and G. E. Scuseria, *J Chem Phys*, 2004, **121**, 1187–1192.

74 J. Heyd, G. E. Scuseria and M. Ernzerhof, *J Chem Phys*, 2006, **124**, 219906.

75 J. Heyd, G. E. Scuseria and M. Ernzerhof, *J Chem Phys*, 2003, **118**, 8207–8215.

76 L. Schimka, J. Harl and G. Kresse, *J Chem Phys*, 2011, **134**, 024116.

77 I. C. Gerber and J. G. Ángyán, *Chem Phys Lett*, 2005, **415**, 100–105.

78 I. C. Gerber, J. G. Ángyán, M. Marsman and G. Kresse, *J Chem Phys*, 2007, **127**, 054101.

79 P. J. Stephens, F. J. Devlin, C. F. Chabalowski and M. J. Frisch, *J Phys Chem*, 1994, **98**, 11623–11627.

80 S. H. Vosko and L. Wilk, *Phys Rev B*, 1980, **22**, 3812–3815.

81 S. L. Dudarev, G. A. Botton, S. Y. Savrasov, C. J. Humphreys and A. P. Sutton, *Phys Rev B*, 1998, **57**, 1505–1509.

82 M. Cococcioni and S. de Gironcoli, *Phys Rev B*, 2005, **71**, 35105.

83 G. H. Gu and D. G. Vlachos, *Journal of Physical Chemistry C*, 2016, **120**, 19234–19241.

84 M. T. Curnan, PhD Thesis, Carnegie Mellon University, 2015.

85 T. Xie, G. R. Wittreich, M. T. Curnan, G. H. Gu, K. N. Seals and J. S. Tolbert, *J Chem Inf Model*, 2025, **65**, 214–222.

86 S. W. Benson and J. H. Buss, *J Chem Phys*, 1958, **29**, 546–572.

87 N. Zhan and J. R. Kitchin, *AIChE Journal*, 2022, **68**, e17516.

88 G. H. Gu, J. Noh, I. Kim and Y. Jung, *J Mater Chem A Mater*, 2019, **7**, 17096–17117.

89 F. Calle-Vallejo, N. G. Inoglu, H.-Y. Su, J. I. Martínez, I. C. Man, M. T. M. Koper, J. R. Kitchin and J. Rossmeisl, *Chem Sci*, 2013, **4**, 1245–1249.

90 Z. Xu and J. R. Kitchin, *Catal Commun*, 2014, **52**, 60–64.

91 V. N. Jafarova and G. S. Orudzhev, *Solid State Commun*, 2021, **325**, 114166.

92 A. Rohatgi, 2024, preprint, 4.7, https://automeris.io/WebPlotDigitizer.

93 D. C. Truong, A. T. T. Pham, O. K. T. Le, D. Van Hoang, T. H. Nguyen, H. K. T. Ta, N. K. Pham, H. T. Lai, T. B. Phan and V. C. Tran, *Science and Technology Development Journal*, 2020, **23**, 788–794.

94 Y.-H. Li, X. G. Gong and S.-H. Wei, *Phys Rev B*, 2006, **73**, 245206.

95 A. Stokes, M. Al-Jassim, D. DIercks, A. Clarke and B. Gorman, *Sci Rep*, DOI:10.1038/s41598-017-14215-0.

96 A. H. Reshak, S. Auluck, I. V. Kityk, Y. Al-Douri, R. Khenata and A. Bouhemadou, *Appl Phys A Mater Sci Process*, 2009, **94**, 315–320.

97 C. Zhao, S. Cui, Y. Li, Y. Wu, T. Li, K. Li, L. Sun, Z. Sun, C. Xiao and Y. Xie, *J Mater Chem A Mater*, 2024, **12**, 23670–23675.

98 K. G. Saw, N. M. Aznan, F. K. Yam, S. S. Ng and S. Y. Pung, *PLoS One*, 2015, **10**, e0141180.

99 A. Hassan, Y. Jin, M. Irfan and Y. Jiang, *AIP Adv*, 2018, **8**, 035212.

100 G. K. H. Madsen, J. Carrete and M. J. Verstraete, *Comput Phys Commun*, 2018, **231**, 140–145.

101 G. K. H. Madsen and D. J. Singh, *Comput Phys Commun*, 2006, **175**, 67–71.

102 M. Wu, D. Sun, C. Tan, X. Tian and Y. Huang, *Materials*, 2017, **10**, 359.

103 C. Kittel and P. McEuen, *Introduction to solid state physics*, John Wiley & Sons, 2018.

104 J. Scheidemantel, C. Ambrosch-Draxl, T. Thonhauser, V. Badding and O. Sofo, *Phys Rev B Condens Matter Mater Phys*, 2003, **68**, 125210.

105 Y. Wang, Y. J. Hu, B. Bocklund, S. L. Shang, B. C. Zhou, Z. K. Liu and L. Q. Chen, *Phys Rev B*, 2018, **98**, 224101.

106 M. Markov, X. Hu, H. C. Liu, N. Liu, S. J. Poon, K. Esfarjani and M. Zebarjadi, *Sci Rep*, 2018, **8**, 9876.

107 M. Oszwaldowski and M. Zimpel, *J. Phys. Chem. Solids*, 1988, **49**, 1179–1185.

108 A. Tsukazaki, A. Ohtomo and M. Kawasaki, *Appl Phys Lett*, 2006, **88**, 152106.

109 C. H. Su, *J Appl Phys*, 2008, **103**, 084903.

110 W. J. Maeng, J. W. Lee, J. H. Lee, K. B. Chung and J. S. Park, *J Phys D Appl Phys*, 2011, **44**, 445305.

111 K. P. Ong, D. J. Singh and P. Wu, *Phys Rev B Condens Matter Mater Phys*, 2011, **83**, 115110.

112 G. El Hallani, M. Khuili, N. Fazouan, A. Liba, H. A. El Makarim and E. H. Atmani, *Chemical Physics Impact*, 2024, **8**, 100648.

113 D. C. Look, D. C. Reynolds, J. R. Sizelove, R. L. Jones, C. W. Litton, G. Cantwell and W. C. Harsch, *Solid State Commun*, 1998, **105**, 399–401.

114 Ü. Özgür, Y. I. Alivov, C. Liu, A. Teke, M. A. Reshchikov, S. Doğan, V. Avrutin, S. J. Cho and H. Morkọ, *J Appl Phys*, 2005, **98**, 1–103.

115 K Ellmer, *J Phys D Appl Phys*, 2001, **34**, 3097.

116 R. Magrin Maffei, A. di Bona, M. Sygletou, F. Bisio, S. D'Addato and S. Benedetti, *Appl Surf Sci*, 2023, **624**, 157133.

117 J. G. Lu, S. Fujita, T. Kawaharamura, H. Nishinaka, Y. Kamada, T. Ohshima, Z. Z. Ye, Y. J. Zeng, Y. Z. Zhang, L. P. Zhu, H. P. He and B. H. Zhao, *J Appl Phys*, 2007, **101**, 083705.

118 T. Pisarkiewicz, K. Zakrzewska and E. Leja, *Thin Solid Films*, 1989, **174**, 217–223.

119 S. P. Ong, W. D. Richards, A. Jain, G. Hautier, M. Kocher, S. Cholia, D. Gunter, V. L. Chevrier, K. A. Persson and G. Ceder, *Comput Mater Sci*, 2013, **68**, 314–319.

120 S. Pal, T. Jasper-Tönnies, M. Hack and E. Pehlke, *Phys Rev B Condens Matter Mater Phys*, 2013, **87**, 085445.